University of Helsinki
Dissertationes Universitatis Helsingiensis
69/2023

ATOMIC LAYER DEPOSITION OF RARE EARTH AND TRANSITION METAL FLUORIDES

Elisa Atosuo

Department of Chemistry
Faculty of Science
University of Helsinki
Helsinki, Finland

DOCTORAL DISSERTATION

To be presented for public discussion with the permission of the Faculty of Science of the University of Helsinki, in Chemicum auditorium A129, A.I. Virtasen aukio 1, on November 3rd, 2023, at 12 o'clock.

Helsinki 2023

Supervisors

Professor Mikko Ritala
Professor Markku Leskelä
Department of Chemistry
University of Helsinki
Helsinki, Finland

Reviewers

Research Director Claudia Wiemer
Institute for microelectronics and microsystems (IMM)
Italian National Research Council
Agrate, Italy

Professor Steven M. George
Department of Chemistry
University of Colorado Boulder
Colorado, United States

Opponent

Associate Professor Tobias Törndahl
Department of Materials Science and Engineering, Solar Cell Technology
Uppsala University
Uppsala, Sweden

Publisher: Helsingin yliopisto
Series: Dissertationes Universitatis Helsingiensis 69/2023

ISBN 978-951-51-9476-3 (print)
ISBN 978-951-51-9477-0 (online)
ISSN 2954-2898 (print)
ISSN 2954-2952 (online)

PunaMusta, Joensuu 2023

Just give me time to find,
Whatever it is, it will be alright.

E-type, Life

ABSTRACT

Atomic layer deposition (ALD) is an advanced thin film deposition method with an essential role in e.g. microelectronics. The assets of ALD are its capability to produce uniform, stoichiometric, and pure films with precise thickness control even on top of complicated structures, such as high aspect ratio trenches. This versatile technique has thus found applications where very thin and continuous conformal films are needed, as well as where particles have to be uniformly coated. The applications of ALD range from protective coatings to solar cells and medical applications. Originally, however, the potential of the method was discovered by the semiconductor industry. ALD-made metal oxides, nitrides, sulfides, and pure metals have therefore been of interest, which is reflected also in the number of ALD processes for these materials. This thesis, in turn, was inspired by the limited amount of basic research on ALD of metal fluorides. In addition to having had no uses in semiconductor industry, ALD metal fluorides have been suffering from the lack of good fluoride precursors.

New ALD processes for rare earth and transition metal fluorides were developed in this work. In addition to the basic research goals, the aim was to provide materials for diverse applications. The applicability of ALD in thin film deposition, particle coating, and luminescent center doping also inspired this work.

The literature section gives an overview of the applications, which for the rare earth metal fluorides are luminescent centers, luminescence host structures, antireflection coatings, and thermal expansion tuning. Of the transition metal fluoride applications, lithium-ion and sodium-ion batteries are covered. The principle of ALD and its use in metal fluoride deposition are presented.

The experimental section summarizes the results of the studied processes: TbF_3, GdF_3, HoF_3, ScF_3, $Sc_xAl_yF_z$, CoF_2, NiF_2, and FeF_x. In general, the rare earth fluoride processes produce crystalline and pure films with ALD characteristics, regardless of the fluoride source used. The transition metal fluoride processes studied: CoF_2, NiF_2, and FeF_x, show more diverse behavior. The best results were obtained with the CoF_2 process which produced stoichiometric films with good ALD characteristics and low impurity contents. The results for the rare earth metal fluorides, especially, are encouraging when thinking about the rare earth fluorides still lacking an ALD process.

PREFACE

The research was done at the University of Helsinki in the HelsinkiALD group.

I want to thank Professor Mikko Ritala and Professor Emeritus Markku Leskelä for giving me the opportunity to do my doctoral research in the ALD group. I also want to thank you for your guidance during the years. I want to thank Professor Matti Putkonen for your advice regarding ALD as well as Dr. Kjell Knapas for advice regarding teaching.

I want to thank the reviewers of this thesis, Research Director Claudia Wiemer and Professor Steven M. George, for their helpful comments.

I also want to thank Associate Professor Tobias Törndahl for accepting the task to serve as the opponent of this thesis.

All my colleagues who have participated and helped in the research are gratefully thanked. I especially want to thank Dr. Miia Mäntymäki for helping me to start my path in the ALD world and later helping me to get more insight on metal fluorides. Mr. Mikko Heikkilä is thanked for your help with the x-ray methods and good discussions. Dr. Miika Mattinen is thanked for the AFM measurements and good discussions about science in general. Dr. Kenichiro Mizohata and Prof. emer. Jyrki Räisänen are thanked for ToF-ERDA measurements, Dr. Marko Vehkamäki for electrical measurements and Dr. Timo Hatanpää for precursor synthesis. My summer trainees, Ms. Laura Keränen, Mr. Juha Ojala, Mr. Leevi Pesonen and Ms. Johanna Majlund, are thanked for their dedication and hard work. Dr. Marianna Kemell is thanked for helping me with the SEM and EDS analysis.

I want to thank all my colleagues for bringing joy in the workdays, especially during the afternoon coffee breaks. I want to thank my former Tietäjät-office mates Georgi, Katja, Miika and Tomi for fun moments and fruitful discussions. I also want to thank my recent office mates Heta, Keränen and Saba for the supporting atmosphere in the office. I want to thank Seniorit, i.e., Mjh and Miia, for your friendship and support during the years. I also want to thank Heta, Juulia and Miika for fun moments also outside work.

Mai, Sofia and Suvi, I am very grateful for your friendship and support since our freshman year. I also want to thank my friend Vilja for all the fun times and discussions about science. Although at very different disciplines, it has been a pleasure to take the academic journey with you. Sara, Anna-Maria and Taru, you have made these stressful years so much funnier!

Finally, I want to thank my family for their love and support and for encouraging me to pursue a PhD.

I am grateful to Kemian Päivien Säätiö, Kordelin Foundation and The Doctoral Programme in Materials Research and Nanoscience (MATRENA) for personal grants. ASM Microchemistry Oy is acknowledged for funding.

CONTENTS

LIST OF ORIGINAL PUBLICATIONS

This thesis is based on the following publications:

I **Atomic layer deposition of TbF_3 thin films**
Elisa Atosuo, Juha Ojala, Mikko J. Heikkilä, Miika Mattinen, Kenichiro Mizohata, Jyrki Räisänen, Markku Leskelä, and Mikko Ritala
J. Vac. Sci. Technol. A, 39 (**2021**) 022404.

II **Atomic layer deposition of GdF_3 thin films**
Elisa Atosuo, Kenichiro Mizohata, Miika Mattinen, Miia Mäntymäki, Marko Vehkamäki, Markku Leskelä, and Mikko Ritala
J. Vac. Sci. Technol. A, 40 (**2022**) 022402.

III **Atomic layer deposition of CoF_2, NiF_2 and HoF_3 thin films**
Elisa Atosuo, Miia Mäntymäki, Leevi Pesonen, Kenichiro Mizohata, Timo Hatanpää, Markku Leskelä, and Mikko Ritala
Dalton Trans. 52 (**2023**) 10844–10854.

IV **Atomic layer deposition of ScF_3 and $Sc_xAl_yF_z$ thin films**
Elisa Atosuo, Mikko J. Heikkilä, Johanna Majlund, Leevi Pesonen, Miia Mäntymäki, Kenichiro Mizohata, Markku Leskelä, and Mikko Ritala
Submitted

The publications are referred to in the text by their roman numerals.

THE AUTHOR'S CONTRIBUTION

I–IV The author designed the study, made most of the depositions and characterizations, and wrote the first version of the manuscript.

OTHER PUBLICATIONS BY THE AUTHOR

1. **Atomic Layer Deposition of CsI and $CsPbI_3$**
   Alexander Weiß, Georgi Popov, Elisa Atosuo, Anton Vihervaara, Pasi Jalkanen, Marko Vehkamäki, Markku Leskelä, Mikko Ritala, and Marianna Kemell
   Chem. Mater. 34 (**2022**) 6087–6097.

2. **Studies on Solid State Reactions of Atomic Layer Deposited Thin Films of Lithium Carbonate with Hafnia and Zirconia**
   Miia Mäntymäki, Elisa Atosuo, Mikko J. Heikkilä, Marko Vehkamäki, Miika Mattinen, Kenichiro Mizohata, Jyrki Räisänen, Mikko Ritala, and Markku Leskelä
   J. Vac. Sci. Technol. A, 37 (**2019**) 020929.

3. **Preparation of Lithium Containing Oxides by the Solid State Reaction of Atomic Layer Deposited Thin Films**
   Elisa Atosuo, Miia Mäntymäki, Kenichiro Mizohata, Mikko J. Heikkilä, Jyrki Räisänen, Mikko Ritala, and Markku Leskelä
   Chem. Mater. 29 (**2017**) 998–1005.

4. **Mn(II) Acetate: an Efficient and Versatile Oxidation Catalyst for Alcohols**
   Minna T. Räisänen, Afnan Al-Hunaiti, Elisa Atosuo, Marianna Kemell, Markku Leskelä, and Timo Repo
   Catal. Sci. Technol. 4 (**2014**) 2564–2573.

5. **In Situ High Temperature X-Ray Scattering Studies on Atomic Layer Deposited Bilayers of A_2CO_3 and MO_x (A = Li/Na, M = Nb/Hf)**
   Elisa Atosuo, Mikko J. Heikkilä, Marko Vehkamäki, Miika Mattinen, Kenichiro Mizohata, Ville Miikkulainen, Markku Leskelä, and Mikko Ritala
   Manuscript.

6. **Atomic Layer Deposition of Cobalt Phosphide Thin Films**
   Elisa Atosuo et al.
   Manuscript.

ABBREVIATIONS

AFM	Atomic force microscopy
ALD	Atomic layer deposition
ALE	Atomic layer epitaxy
ARC	Antireflection coating
a-Si	Amorphous silicon
a.u.	Arbitrary units
c-Si	Crystalline silicon
CTE	Coefficient of thermal expansion
CVD	Chemical vapor deposition
EDS	Energy dispersive x-ray spectroscopy
ESA	Excited states absorption
ETU	Energy transfer upconversion
EXAFS	Extended x-ray absorption fine structure
FESEM	Field emission scanning electron microscopy
GI-XRD	Grazing incidence x-ray diffraction
GPC	Growth per cycle
Hfac	Hexafluoroacetylacetonate
HMDS	Bis(trimethylsilyl)amide
HTXRD	High temperature x-ray diffraction
HTXRR	High temperature x-ray reflection
IBS	Ion-beam sputtering
ITO	Indium tin oxide
MRI	Magnetic resonance imaging
PMMA	Polymethyl methacrylate
PVD	Physical vapor deposition
XRD	X-ray diffraction
RBS	Rutherford backscattering spectrometry
Rms	Root mean square
SOFC	Solid oxide fuel cell
Thd	2,2,6,6-tetramethyl-3,5-heptanedione
TMA	Trimethylaluminum
TMEDA	N,N,N′,N′-tetramethylethylenediamine
TMPDA	N,N,N’,N’,-tetramethyl-1,3-propanediamine
ToF-ERDA	Time-of-flight elastic recoil detection analysis
UV	Ultraviolet
UV-Vis	Ultraviolet-visible
XRR	X-ray reflection
ZTE	Zero thermal expansion

1 INTRODUCTION

Atomic layer deposition (ALD) is a sophisticated thin film deposition method that can produce continuous, pure, stoichiometric, and uniform conformal films with extremely good thickness control, also on complicated structures.[1] Due to the versatility of the method, it is used in many applications such as solar cells, protective coatings, and optical applications.[2–4] However, ALD is probably best known from its role in the information technology: the adoption of ALD enabled the semiconductor industry to take a huge leap in the first decade of 2000's.[Ref. 5] It is often stated that ALD was and will be the enabler of keeping up with the Moore's law by allowing the manufacture of smaller and smaller components.

Since the turn of millennium, the number of materials deposited with ALD has grown fast. Today, ALD processes cover many simple but important semiconductor industry materials such as metal oxides, sulfides and nitrides, and pure metals.[6] ALD research has reached a stage where most developments are made in deposition of quaternary materials and electropositive metals as well as fine-tuning the existing processes to meet the requirements of industrial applications. Despite the success in ALD of the advanced materials, there are some groups of simple materials which are lagging behind in the basic research. One of these groups is metal fluorides.

The lack of ALD processes for metal fluorides is related to the lack of suitable fluoride precursors, but also to the lack of applications in semiconductor industry. From the fluoride precursor perspective, the main challenge is to find a good replacement for the efficient but toxic hydrogen fluoride. Often, the use of milder ALD precursors has come at the expense of the purity of the films.

Nowadays, the potential of metal fluoride thin films has been recognized in e.g. antireflection coatings and lithium-ion and sodium-ion batteries.[7–9] Rare earth fluorides, especially, have future applications also in nanoparticle form, e.g., in medical applications.[10] ALD could provide good-quality thin films for both the application types. Moreover, with ALD it is possible to uniformly dope ions into a film. This is an important property with respect to luminescence devices, which is one of the most important applications for rare earth fluorides.

The aim of this theses was to develop new ALD processes for rare earth and transition metal fluorides. The materials were selected so that many kinds of applications were covered. The thesis presents ALD processes for TbF_3, GdF_3, CoF_2, NiF_2, HoF_3, ScF_3, and $Sc_xAl_yF_z$. Chapters 2–3 discuss the applications of selected rare earth and transition metal fluorides, also including potential future applications. Chapter 4 introduces the ALD method and reviews the existing ALD processes for metal fluorides. Chapter 6 presents the main

findings of each studied ALD process and reports also unpublished and unsuccessful ALD studies. The conclusion chapter 7 summarizes the work and gives thoughts on future research directions.

2 RARE EARTH FLUORIDE APPLICATIONS

The group of rare earth metals consists of the elements Sc, Y, and the lanthanides (La-Lu). These metal ions are small and electropositive, and bond favorably with the hard fluoride ions. Bonding in the rare earth metal fluorides is ionic which together with the low polarizability of the ions leads to high band gaps and low refractive indices. When these properties are combined with the intrinsic good stability and low hygroscopicity, attractive materials especially for antireflection coatings are obtained. In addition, thanks to the extraordinary light emitting properties of the lanthanide ions, applications in luminescence devices are also found.

2.1 ANTIREFLECTION COATINGS

There are numerous devices where the reflection of light needs to be suppressed. Antireflection coatings (ARCs) are needed for example in cameras, microscopes, solar cells, telescopes, and photolithography. ARCs are used to suppress annoying reflections, improve contrast, and increase transmission. In this chapter, the basic principles of minimizing reflection and absorption are discussed, omitting the complicated physics, however.

Figure 1 shows a substrate that has been coated with an AR coating. The R vectors denote the light reflected from the surface without entering the film (R_1) and the light reflected from the AR coating/substrate interface (R_2). The role of an AR coating is to make the two reflections to cancel each other. Both the physical thickness of the AR coating and the refractive indices of the materials have to be considered.[11]

In the case of light coming from a medium with a lower refractive index to a medium with a higher refractive index, the phase of the reflected light changes by 180°. In Figure 1, n_a denotes the refractive index of air, n_s of the substrate, and n_f of the coating. If the refractive indices are in the order $n_a<n_f<n_s$, there is a 180° phase change both when the light reflects from the air/film interface and the film/substrate interface. To cancel out the reflections, the path length difference of the light has to be $\lambda/2$. However, the change in the refractive index causes a change in the wavelength of the light: in a film with the refractive index n_f, the wavelength is λ/n_f. The physical thickness of the AR coating needed to obtain the desired phase change is obtained most conveniently by considering the optical thickness ($n_f d_f$) of the film that must equal $\lambda/4$. This gives a physical thickness as shown in Equation 1.[Ref. 11]

$$(1) \qquad d_f = \frac{\lambda}{4n_f}$$

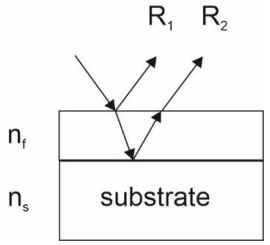

Figure 1 The role of an AR coating is to make the reflections R_1 and R_2 to cancel out each other.

For the intensity of the reflected light to be zero, also the amplitude of the light must be considered. Equation 2 gives the relation of the refractive indices of the substrate and the film to obtain zero reflectance when light is coming in an angle perpendicular to the surface.[11]

$$(2) \qquad n_f = \sqrt{n_s n_a}$$

For air, the refractive index is 1.00. Hence, in the case of glass (n_s=1.52) it should be coated with a material with a refractive index of 1.23 for the reflectance to be zero. In practice, the lowest achievable refractive index for a dense coating is 1.38 of magnesium fluoride, and MgF_2 is thus commonly used. A $\lambda/4$ MgF_2 coating is able to reduce the reflection of light on glass from 4 % without the coating to < 1.3 %. It should be noted that in general the refractive index of a material can be lowered by making the coating less dense, i.e., by introducing pores in the coating.[12]

Note that the $\lambda/4$ optical thickness can be achieved only with one wavelength. Similarly, the thickness is optimized only for one incident angle of light. At other wavelengths or incidence angles, the total path travelled by the light is different, and thus the reflections are not completely canceling out each other. When antireflection properties are needed over a wide wavelength range or wide angles of incidence light, special multilayer coatings have to be designed.[13]

In turn, when very low reflectance at one wavelength is needed, a stack of low and higher refractive index material layers of $\lambda/4$ optical thickness are used. The optimal ratio of the refractive indices of the materials are dictated by Equation 3, when light propagates from air to the material with a low refractive index (n_L) and then to the material with a higher refractive index

(n_H). For example, in the case of a glass substrate and MgF_2 as the low index material, the refractive index of the other material should be 1.70.[Ref.13]

$$\frac{n_L^2}{n_H^2} = \frac{1.00}{n_S} \quad (3)$$

In the work by Yoshida et al. MgF_2 and GdF_3 layers were deposited on both sides of a CaF_2 substrate by ion-beam sputtering (IBS) as shown in Figure 2.[Ref. 14] Transmittance as high as 99.7% was obtained at the wavelength of 193 nm. Without the coating the transmittance was ~93%. The motivation for this study was to create antireflection coatings for 193 nm lasers in deep ultraviolet (DUV) lithography.

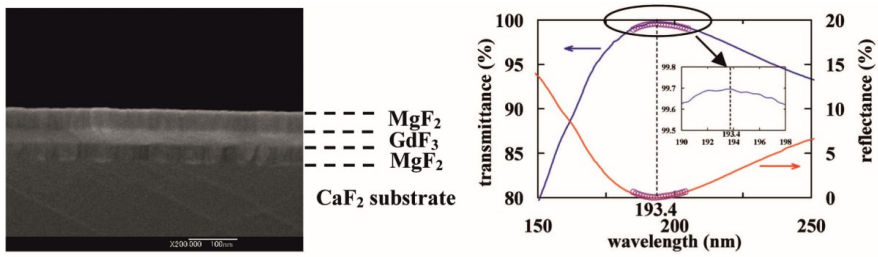

Figure 2 Cross-section SEM image of the MgF_2/GdF_3 multilayer coating and the measured (line) and calculated (open circle) transmittance and reflectance of a MgF_2/GdF_3 multilayer structure. Reproduced with permission from Ref. 14, Copyright 2006 The Optical Society.

When eliminating reflections with antireflection coatings, usually it is essential also to avoid absorption of light in the coating. Transparent antireflection coatings are needed for example in lenses in photolithography, cameras, and eyeglasses. If the AR coatings are to be used at the UV wavelengths, the absorbance of e.g. oxides becomes remarkable. Contrary to oxides, alkali metal fluorides, alkaline earth metal fluorides, and rare earth fluorides have high band gaps and are thus suitable AR coatings also for the UV wavelengths. In practice, alkaline earth metal fluorides and rare earth fluorides are more suitable than alkali metal fluorides due to their better stability in atmospheric conditions.

In addition to reflection and absorption, also scattering of light affects the antireflection properties of the coating. In principle, the smoother the coating is, the less scattering of light is occurring. The AR coating manufacturing method has thus a major role in eliminating the scattering losses.

Other general demands for the AR deposition method are the ability to produce pure films to decrease the amount of light absorbing impurities. The

film thickness controllability should be extremely good. Also, coating non-planar objects such as lenses uniformly and conformally should be possible. Traditionally, physical vapor deposition (PVD), chemical vapor deposition (CVD), and sol-gel methods have been popular in antireflection coating deposition, but given the unique properties of ALD, it is likely to become more popular in coming years.

2.2 RARE EARTH LUMINESCENCE

The applicability of rare earth ions, or more precisely lanthanides, as colorful light producing systems is based on their extraordinary electronic structure. In the periodic table, lanthanides are the elements in which the 4f orbitals start to be occupied. For example, in elemental terbium the electron configuration is [Xe] $4f^9\ 5d^0\ 6s^2$ and in the terbium 3+ ion it is [Xe] $4f^8\ 5d^0\ 6s^0$. The 4f electrons of lanthanides are shielded by the 5s and 5p electrons and consequently only weakly coupled with matrix phonons.[15] This results in discrete energy levels and sharp 4f-4f transitions. In many lanthanide ions, the most interesting 4f-4f transitions occur at visible wavelengths, e.g., green for Tb^{3+}, red for Eu^{3+}, and blue for Tm^{3+}. Due to the shielding by the outer electrons, the effect of the chemical environment on the energy of 4f levels is also very weak. Thus, the energies of the 4f-4f transitions – and therefore the color of the emitted light – are similar in different kinds of chemical environments.

Because the 4f-4f transitions are forbidden by the Laporte rules, the absorption coefficients for these transitions are low.[15] Therefore, the luminescent centers usually need to be accompanied by sensitizer ions. An example of this is the Ce^{3+}/Tb^{3+} pair. In this system, UV light is first absorbed by the Laporte allowed 4f-5d transitions in the Ce^{3+} ions, and the energy is then transferred non-radiatively to Tb^{3+}. The characteristic green light emission occurs when the terbium ions relax radiatively (Fig. 3).

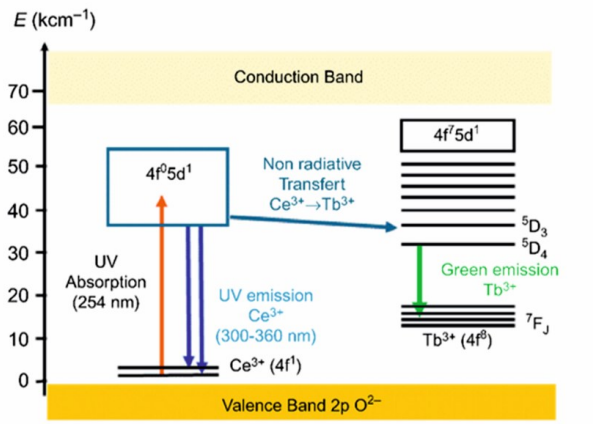

Figure 3 Exciting light is absorbed by the Laporte allowed 4f–5d transition in Ce^{3+}, and the energy is then transferred to Tb^{3+} ions from which the green light emission occurs. Reproduced with permission from Ref. 16, Copyright 2015 Elsevier.

The transfer of energy between rare earth ions is nicely demonstrated also in upconversion and downconversion processes. In an anti-Stokes process called upconversion, two or more photons of low energy, e.g., near infrared (NIR), are converted to one photon of higher energy, e.g., visible light. The upconversion process can occur in systems where only one type of active ions is present but also with the help of sensitizer ions. For the upconversion to occur, there must be a long-lived, metastable intermediate state available. The most common mechanisms[17] are presented here:

1) In a one-ion system, the low energy photon is first absorbed by the active ion that is excited to the intermediate state. Subsequently, another photon is absorbed, and the ion is excited from the intermediate state to an even higher energy level. The overall outcome is that the energy finally emitted by the ion is higher than the energy of the originally absorbed photons. This mechanism is known by the name excited states absorption (ESA). The ESA mechanism is schematically presented in Figure 4a.

2) In the sensitizer-activator process, two (or more) sensitizer ions absorb one photon each and excite to higher energy levels. One sensitizer ion then transfers the energy non-radiatively to the active ion so that the active ion is excited. This is followed by a second non-radiative energy transfer from another sensitizer ion to the active ion, and the active ion is excited to a higher energy level. This process is called energy transfer upconversion (ETU). The ETU mechanism is schematically presented in Figure 4b.

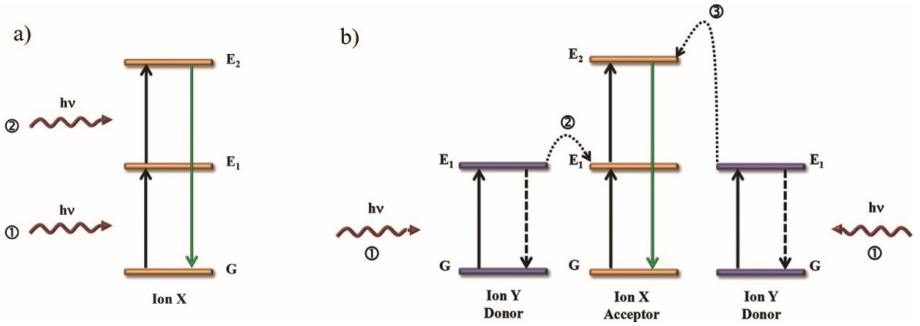

Figure 4 The upconversion mechanisms of a) excited states absorption (ESA) and b) energy transfer upconversion (ETU). Reproduced with permission from Ref. 17, Copyright 2015 John Wiley and Sons.

In the downconversion, the absorption of a high energy photon eventually results in the emission of two or more low-energy photons. There are several ways how the downconversion can occur[18], e.g.:

1) An excited sensitizer ion transfers some of its energy to the activator, which then relaxes producing (usually) visible light. The remaining energy in the sensitizer can then be transferred to a second activator ion, followed by visible light emission.

2) The sensitizer first transfers energy to the activator as in the case 1) but then emits itself the remaining energy instead of transferring it to a second activator ion.

3) The sensitizer ion first emits a visible photon, and then transfers the remaining energy to the activator.

A drawback of the energy transfer between lanthanides is the luminescence quenching. If the concentration of the luminescent centers is too high, the probability for non-radiative relaxation between neighboring lanthanides increases. Therefore, the luminescent centers are always embedded in a host structure to ensure sufficient distance between them.[19]

Although the chemical environment has very weak effect on the individual emission lines, the host structure should be chosen carefully. The main reason is again related to de-excitation. If the host structure has high phonon energies (lattice vibration energies), the de-excitation might occur non-radiatively through coupling with the host lattice vibrations. Good host structures are for example metal fluorides which have in general low phonon energies and high thermal and chemical stability. In addition to the low phonon energies, the cation of the host fluoride should preferably be of the same size as the active ion, such as in $NaYF_4$, to reduce lattice defects and stress.[19] In practice, the

extent of the luminescence quenching is also determined by for example the purity, crystal phase, and morphology of the host material.[19]

In addition to light as discussed above, luminescence can be excited by the impact of, e.g., electrons, ionizing radiation, friction, or pressure on the material. The most convenient and widespread ways to excite the rare earth ions are electrons and photons. For electroluminescence, perhaps the most well-known application is electroluminescent displays, where also TbF_3 embedded in ZnS has been studied as a luminescent center.[20] However, as fluorides are intrinsically poor electronic conductors and thus not in general suitable for electroluminescence, those applications are not covered in this thesis. Rather, this work concentrates on photoluminescence applications. Examples of possible applications are presented in the following chapters.

2.2.1 SOLAR CELLS

Rare earth fluorides have at least two applications in solar cells. They can serve as an upconversion or downconversion material, and as an electron-selective contact. Although not related to photoluminescence, also the second application is presented in this chapter.

In general, no matter which solar cell technique is in question, one of the limiting factors is that only a limited range of the Sun's spectrum can be efficiently converted to energy. The photons that have lower energy than the semiconductor bandgap are not absorbed. In turn, the photons having higher energy than the band gap form hole–electron pairs, but the excess energy is lost as heat. Rare earth upconversion and downconversion can be used to improve the efficiency of solar cells. Studies on the use of rare earth fluorides in at least amorphous silicon solar cells (a-Si), dye-sensitized solar cells (DSSCs), and organic solar cells (OSC) have been published.[21]

As an example of an upconversion system, Cheng et al. synthesized $NaGdF_4:Yb^{3+},Er^{3+}$ microcrystals for a-Si solar cells[22] where the high wavelength limit for the absorption of light is 708 nm.[Ref.21] Upon illuminating the $NaGdF_4:Yb^{3+},Er^{3+}$ microcrystals with 980 nm light, the energy is first absorbed by the Yb^{3+} ions and then transferred to the Er^{3+} ions. The wavelength of the light finally emitted by the Er^{3+} ions is in the range of ~435–654 nm and can thus be absorbed by the a-Si solar cell. In the solar cell structure, the $NaGdF_4:Yb^{3+},Er^{3+}$ microcrystals were embedded in polymethyl methacrylate (PMMA). The best results were obtained when the upconversion layer was placed on the rear side of the solar cell and combined with a back reflector (Fig. 5). With this configuration, the number of photons emitted towards the solar cell was maximized, and 10-fold enhancement in the photocurrent compared to a solar cell without the UC layer was measured. A downconversion system can be constructed from the same host, $NaGdF_4$, with e.g., Eu^{3+} as the active ion.[23] Gd^{3+} ions act as sensitizers for the active ion.

Naturally in the case of the downconversion the layer must be placed in front of the absorber.

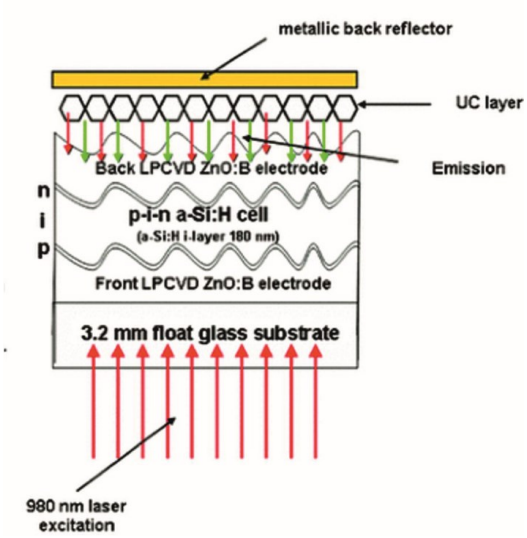

Figure 5 A schematic of a a-Si solar cell with an upconverting $NaGdF_4$:Yb^{3+},Er^{3+}/PMMA layer and a back reflector.[22] Reproduced with permission from Cheng, R. et al. Citric Acid-Assisted Growth of Lanthanide Ions Co-Doped One-Dimensional Upconversion Microcrystals and Their Photovoltaic Applications. J. Mater. Sci. Mater. El. 25, 4066–4073 (2014). Copyright 2014 Springer Nature. http://www.springer.com/journal/10854

Rare earth fluorides have recently found new application as electron-selective contacts in crystalline silicon solar cells (c-Si). Passivating contacts are needed in between the c-Si and the metal electrodes to suppress the recombination of electrons and holes. Usually, a thin Si layer doped with phosphorus has been used on the collector. However, doping with phosphorus adds complexity and hazards in the manufacturing process, and also parasitic absorption of light is an issue.[24] Rare earth fluorides as contacts could provide simple manufacturing, less parasitic absorption, and good electron selectivity. At least YF_3, CeF_3, EuF_x, and GdF_3 have been reported as possible contact materials.[25–28] For example, in the work by Chen et al., GdF_3 films were deposited by thermal evaporation in between the n-Si and Al in a partial rear-contact c-Si solar cell (Fig. 6a).[28] The 1.4 to 5.6 nm thick GdF_3 films improved the power conversion efficiency from 17.40 to 20.71% as compared to the n-Si/Al structure without the GdF_3 layer (Fig. 6b).

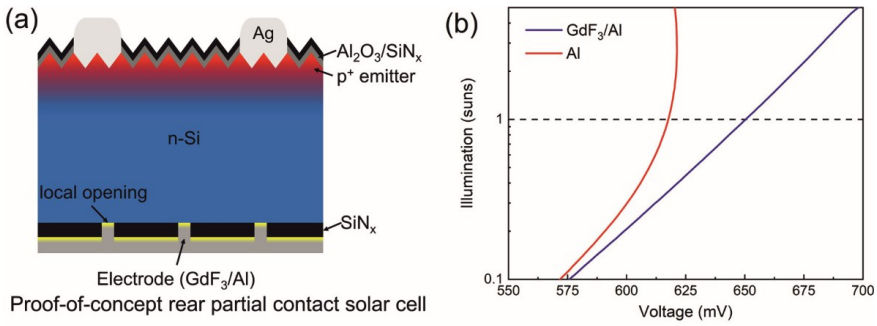

Figure 6 a) Schematic of a GdF_3/Al electrode as a partial rear contact in crystalline silicon solar cell and b) the open circuit voltage of the solar cell with and without the GdF_3 layer.[28] Reproduced with permission from Chen, N. et al. Gadolinium Fluoride as a High-Thickness-Tolerant Electron-Selective Contact Material for Solar Cells. ACS Appl. Energy Mater. 5, 4351–4357 (2022). Copyright 2022 American Chemical Society.

2.2.2 ANTICOUNTERFEITING

Combinations of different emission lines of the lanthanides can be utilized in security applications, such as in bank notes and tags for documentation. The idea is to create a complex optical fingerprint consisting of several rare earth emission lines. Upon illumination, the object under investigation emits its characteristic luminescence pattern. The emission is then compared to the emission pattern of the known reference.

The operation principle of anticounterfeiting tags can be divided into two groups according to the complexity of the security mechanism.[29]

1) single-level luminescence
2) multi-level luminescence

1) In single-level luminescence, the security tag is inspected in one step. For example, the tag under inspection is illuminated at one wavelength and, after an upconversion process, several emission lines are seen. The exact color of the emission is dependent on the concentration of the luminescent centers. Creating new tags is relatively straightforward. However, forging the patterns is not overly complicated.

2) Multi-level luminescence utilizes many inspection steps. These can involve illumination by different wavelengths or illumination power or exposure to elevated temperatures etcetera. Luminescence lifetime may also be exploited. It is clear that mimicking the complicated luminescence pattern is troublesome, but so is the designing of it.

Even though the combinations used in real application are not disclosed, the outcome of illuminating lanthanide doped $NaREF_4$ microrod/core-shell particle hybrids was nicely presented in the article by Hu et al.[30] A change in the emission color was obtained by a temperature increase (Fig. 7). In the work by Zhao et al., $NaYF_4:Yb^{3+}$, Er^{3+} was made in thin film form by electrodeposition, and the possibility to use it in anticounterfeiting applications was suggested.[31] Dong et al., in turn, made flexible anticounterfeiting labels by preparing $NaGdF_4:Yb^{3+},Er^{3+}$@carbon dot nanoparticles by a solvothermal method and depositing those on cellulose films.[32]

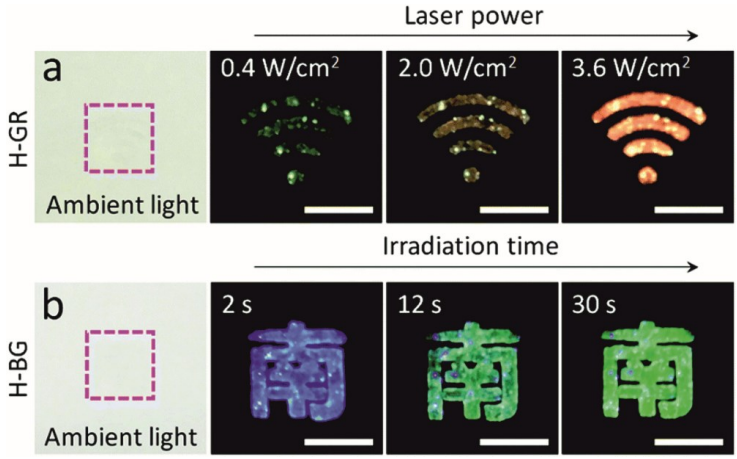

Figure 7 Luminescence recorded from $NaREF_4$ microrod/core-shell particle hybrids a) doped with Ce^{3+}, Ho^{3+}, Er^{3+}, and Yb^{3+} and illuminated with different laser power densities and b) doped with Er^{3+}, Tm^{3+}, and Yb^{3+} and exposed to different irradiation times. In both cases, the color change is caused by the increasing temperature of the material upon irradiation. Reproduced with permission from Ref. 30, Copyright 2019 Royal Society of Chemistry.

2.2.3 SOLID STATE LIGHTING

Solid state lighting is an emerging application for rare earth photoluminescence. The motivation stems from the need for energy efficient and high-quality sun-light mimicking light for, e.g., display backlights and lighting in general.

In solid state, white light can be generated by combining emission of three LEDs: red, green, and blue (Fig. 8a). The drawback of this approach is however that it is intolerant to changes in individual LEDs. Alternatively, white light can be generated by using a blue LED and a yellow phosphor (Fig. 8b), but this approach produces cold white light. A third option is to use blue (Fig. 8c) or UV LED (Fig. 8d) in combination with phosphors that emit red, green, (and blue) light. Rare earth ions embedded in a fluoride matrix can offer bright emission of different colors for this purpose. In addition, if needed, the tone of the white light can be tuned by adjusting the rare earth dopant concentrations.[33,34]

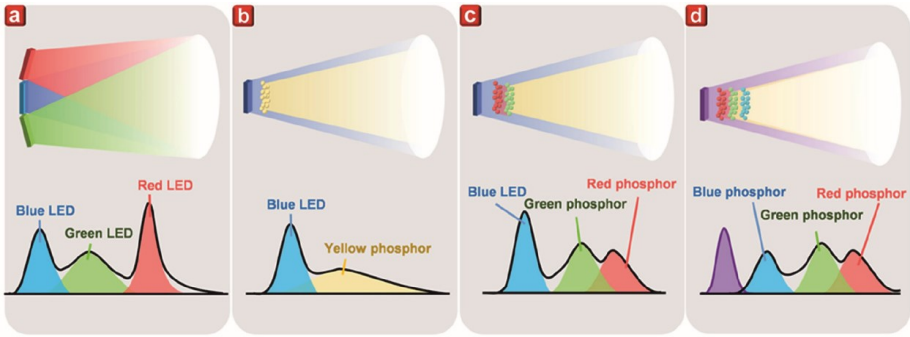

Figure 8 White light can be generated by combining a) red, green, and blue LEDs, b) blue LED and a yellow phosphor, c) blue LED and red and green phosphors, or d) UV LED and red, green, and blue phosphors. Reprinted with permission from Ref. 34, Copyright 2022 American Chemical Society.

Sayed et al. produced white light by Eu^{3+}, Tb^{3+} and Dy^{3+} doped CeF_3 nanoparticles.[35] The best results were obtained with the doping contents of 2.0 mol% of Tb^{3+}(green), 3.5 mol% of Dy^{3+} (blue), and 4.5 mol% of Eu^{3+} (red). When the material was illuminated with a UV lamp, daylight like emission was obtained. To mimic the structure of a solid-state lighting device, a transparent nanocomposite was made by embedding the CeF_3:Tb^{3+},Dy^{3+},Eu^{3+} nanoparticles in PMMA. Bright emission upon UV illumination was observed also in this case.

It is possible to create a white light emitting phosphor system also by doping one kind of a rare earth ion with many emission lines into a host structure (Fig. 9). Li et al. made Eu^{3+} doped GdF_3 nanofibers and illuminated these with UV light.[36] By adjusting the Eu^{3+} content, light emission from blue

to white and red was observed. The color changes are due to the different concentration quenching behavior of the emission lines.

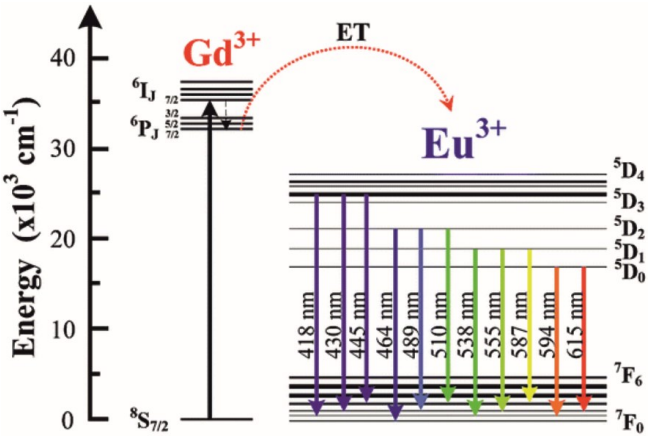

Figure 9 Eu^{3+} doped GdF_3 absorbs UV light and transfers energy to the Eu^{3+} ions. The emission spectrum of the Eu^{3+} ions is concentration dependent. Reproduced with permission from Ref. 36, Copyright 2016 Royal Society of chemistry.

2.2.4 BIOIMAGING

Rare earth fluoride-based nanoparticles have been studied as substituents for organic dyes and quantum dots in bioimaging. Their benefits are photostability, chemical robustness, long luminescence lifetime, and low toxicity.[37,38] For the bioimaging purposes, the rare earth fluoride nanoparticles can be attached to organic molecules that are tailored to bind to specific targets, e.g., tumors. These particles are delivered into tissues and once they have reached the target, they are illuminated. The resulting luminescence is then recorded, giving information about the tumor (Fig. 10).

Rare earth fluoride nanoparticles such as $NaGdF_4$ that upconvert NIR light to visible light have gained a lot of attention. Biological tissues absorb the least in the NIR range, and therefore NIR light can penetrate deeper in the tissues than UV and visible light. In addition, using NIR light for the excitation gives rise to less autofluorescence and hence enhanced image contrast.[38] Especially interesting research was done by Vetrone et al. who coated the upconverting $NaGdF_4:Er^{3+},Yb^{3+}$ nanoparticles with a $NaGdF_4:Yb^{3+}$layer.[39] As compared to the uncoated particles, the luminescence yield was improved because the nonradiative quenching on the surface defects was suppressed. Also the Yb^{3+} ions in the $NaGdF_4:Yb^{3+}$layer served as additional sensitizers. The coating of the nanoparticles was done by solution methods, but the study is inspiring also from the ALD point of view.

Compared to other rare earth fluorides, gadolinium-based host structures have additional advantages due to their magnetic properties. Gd^{3+} containing

bioimaging host materials can simultaneously serve as contrast agents for magnetic resonance imaging (MRI). Gd^{3+} has seven unpaired electrons, large magnetic moment, and long electronic relaxation time. It thus efficiently reduces proton relaxation times in water molecules, improving contrast between healthy and diseased tissues.[40,41]

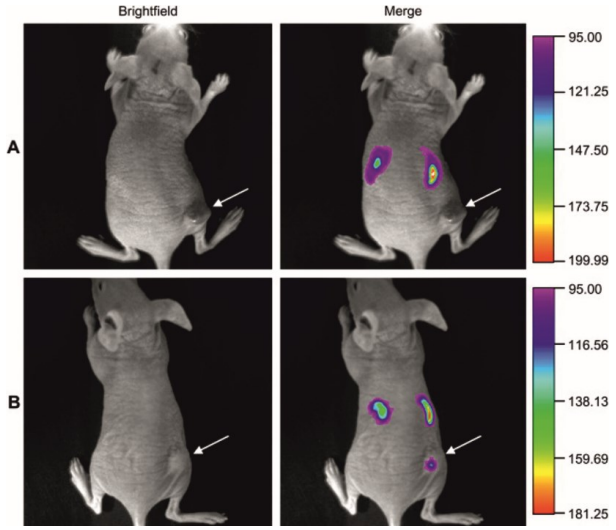

Figure 10 $NaYF_4:Yb^{3+},Er^{3+}$ nanoparticles with different functionalization in A and B. In B, the nanoparticles accumulate in the tumor, which is marked by the white arrow.[42] Reprinted from Biomaterials Vol. 30, Xiong, L. Q., Chen, Z. G., Yu, M. X., Li, F. Y., Liu. C. & Huang, C. H. Synthesis, Characterization, and In Vivo Targeted Imaging of Amine-Functionalized Rare-Earth Up-Converting Nanophosphors., 5592–5600, Copyright (2009) with permission from Elsevier. http://www.sciencedirect.com/journal/biomaterials

2.3 NEGATIVE THERMAL EXPANSION

A unique member of the rare earth fluorides is scandium fluoride. Instead of optical applications, the focus is on its extraordinary thermal behavior. Scandium fluoride is one of the rare examples of materials that possess a negative thermal expansion coefficient, i.e., it contracts upon heating. In addition, the contraction is observed over a wide temperature range, approximately from 10 to 1100 K. Research on both the fundamental properties of ScF_3 as well as tuning of the thermal properties has been active ever since the negative thermal expansion of ScF_3 was experimentally proved by Greve et al. in 2010.[Ref. 43]

The cubic phase of ScF_3 consists of corner-sharing $[ScF_6]$ octahedra, which form a ReO_3-type crystal structure, similar to many other negative thermal expansion materials (Fig. 11a). By using powder x-ray diffraction (XRD), Greve et al. verified that the negative thermal expansion is encountered also in ScF_3.[Ref.43] They suggested the behavior to result from transverse vibrations of

the fluoride ions and rocking motion of the [ScF_6] octahedra. Later, thermal properties of ScF_3 have been studied with e.g. neutron scattering, diffuse x-ray scattering, and extended x-ray absorption fine structure (EXAFS).[44–46] It has been shown that the contraction of the structure upon heating is indeed a result of the tilt of the [ScF_6] octahedra simultaneously with the distortion of Sc-F bonds. The thermally induced vibrations of the fluoride ions occur mainly perpendicular to the Sc–F–Sc bonds, resulting in a guitar string like motion. The scandium ions are pulled closer to the central fluoride and hence closer to each other. Simultaneously, the octahedra tilt towards the center void as illustrated in Figure 11b.

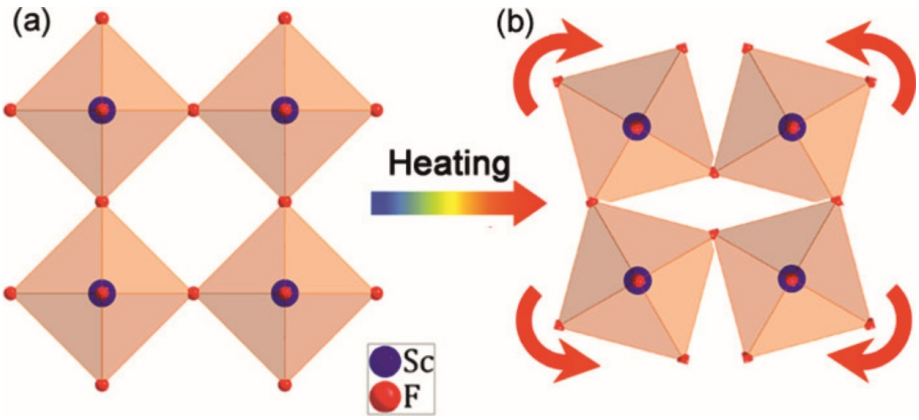

Figure 11 The structure of cubic ScF_3 a) at room temperature and b) upon annealing. Reproduced with permission from Ref. 47, Copyright 2017 American Chemical Society.

Besides the cubic ScF_3, also the hexagonal form of ScF_3 shows negative thermal expansion.[48] Hexagonal ScF_3 consists of [ScF_6] octahedra as well, but they form hexagonal rings with voids in the middle (Fig. 12). Also in the hexagonal phase, tilt of the octahedra has been observed upon annealing. However, as opposite to the cubic form, the slight distortion is preserved in the structure after the material cools down.

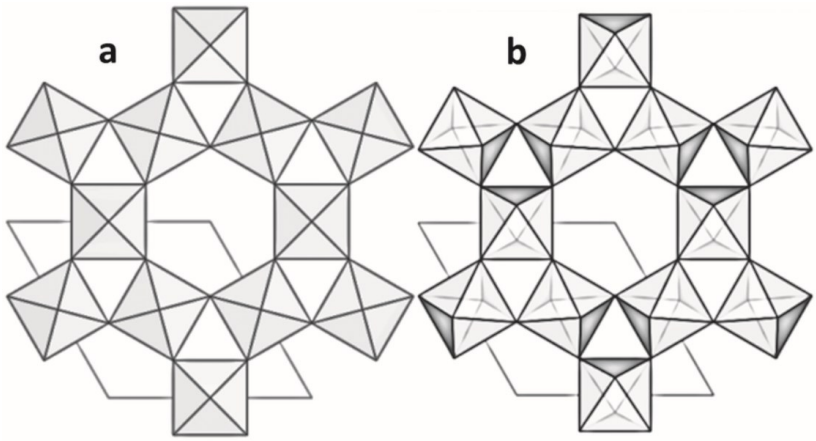

Figure 12 Structures of a) undistorted and b) distorted hexagonal ScF_3. The tilt angle is exaggerated to better show the tilt. Reproduced with permission from Ref. 48, Copyright 2018 Royal Society of Chemistry.

In devices operating at elevated temperatures, different thermal expansions of materials induce stress. Deformation caused by the stress can have detrimental effects on the performance of the devices, especially in high precision applications such as optical mirrors.[49] In semiconductor industry, an important challenge is the thermal mismatch of silicon and other components such as heat sinks.[49] Extreme-case examples of thermal compatibility challenges are solid oxide fuel cells (SOFC) which operate at temperatures as high as 1000 °C, and demand compatibility of the thermal properties of electrodes, electrolytes, and interconnects.[50]

Negative thermal expansion materials offer a way to counteract the common expansion. By combining them with positive thermal expansion materials, the expansion can be suppressed, and even zero thermal expansion (ZTE) materials can be obtained. Several approaches have been taken to modify also the thermal expansion coefficient of ScF_3. Doping of ScF_3 with at least Y^{3+}, Ti^{3+}, Al^{3+}, Fe^{3+}, Zr^{4+}, and Fe^{3+} + Ga^{3+} has been studied.[47,51–55] The replacement of scandium ions with other cations leads to distortions of the structure and therefore changes in the thermal behavior. With a careful choice of the doping ratio, close to zero thermal expansion coefficients have been obtained. As an example, Morelock et al. synthesized $Sc_{1-x}Al_xF_3$ by a solid-state reaction of ScF_3 and AlF_3 powders and obtained close to zero thermal expansion at the temperature range of ~600 to 800 K with x= 0.15.[Ref. 53]

Another approach for creating a ZTE material is to construct a composite structure from ScF_3 and a positive thermal expansion material. Xiao et al. created a ScF_3@Cu core-shell structure by plating copper on ScF_3 particles.[56] They reported thermal expansion and thermal conductivity as a function of the copper content (Fig. 13). With 40 % Cu volume fraction (ScF_3@Cu-40), a coefficient of thermal expansion (CTE) close to that of silicon was obtained.

Importantly, the thermal conductivity of the core-shell structures is also good, making these structures interesting heat sink materials for integrated circuits.

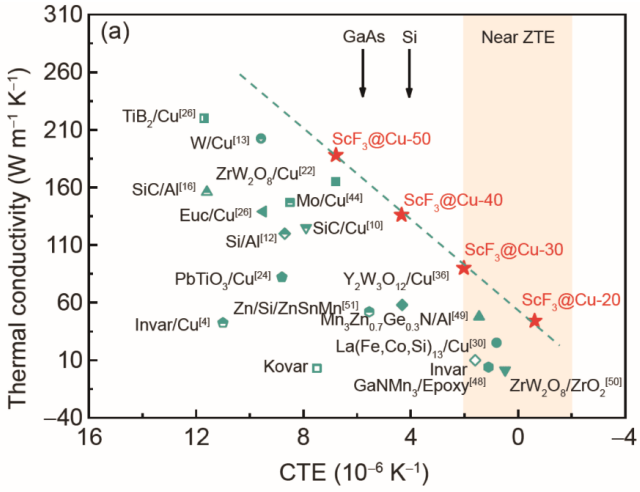

Figure 13 Thermal conductivities and thermal expansion coefficients of ScF_3@Cu core-shell composites and other negative thermal expansion materials.[56] Reproduced with permission from Xiao, N. et al. Realization of high thermal conductivity and tunable thermal expansion in the ScF_3@Cu core-shell composites. Sci. China Technol. Sci. 64, 2057–2065 (2021). Copyright 2021 Springer Nature. http://www.springer.com/journal/11431

3 TRANSITION METAL FLUORIDES AS CONVERSION CATHODES

One of the most studied applications for transition metal fluorides are lithium-ion and sodium-ion batteries. Rechargeable lithium-ion batteries (LIBs) are considered as the best energy storage system for example in transportation due to their excellent energy density and long cycle life.[57] An analogous system to the lithium-ion battery is sodium-ion battery. Interest towards sodium-based energy storage has risen especially thanks to the abundance of sodium.[58]

Lithium-ion batteries consist of a cathode, an anode, an electronically insulating electrolyte, a separator, and current collectors. The operation principle of a rechargeable lithium-ion (and sodium-ion) battery is as follows: when the battery is fully charged, lithium ions reside on the anode. Once no voltage is applied, lithium ions move from the anode to the cathode through the electrolyte. Energy is obtained from the system when electrons move from the anode to the cathode through an external circuit to balance the charge inequilibrium caused by the movement of lithium ions (Fig. 14). This reaction is spontaneous and driven by an intercalation reaction of the cathode. Once the maximum amount of Li^+ ions are occupying the cathode sites, the battery is out of charge. To charge the battery again, the movement of Li^+ ions has to be reversed, i.e., a potential has to be applied to the cell. When no potential is applied, and the cell is connected to an external device, spontaneous Li^+ ion movement follows once again.

Typical cathode materials in LIBs are for example $LiCoO_2$ and other layered oxides. Graphite is widely used as the anode. The electrolytes are either liquid or solid materials, such as $LiPF_6$ in organic solvent or solid lithium phosphorus oxynitride (LiPON). The current collectors can be made of, e.g., copper and aluminum.

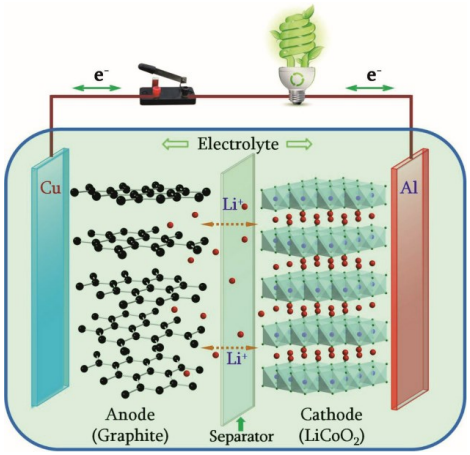

Figure 14 Schematic presentation of a lithium-ion battery with an intercalation cathode. Reprinted with permission from Ref. 59, Copyright 2016 Authors, distributed under a Creative Commons Attribution (CC BY-NC-ND) License. https://doi.org/10.1016/j.mattod.2015.10.009

The energy densities of the current batteries are mostly limited by the cathodes, and therefore cathode research is active. In addition to the high energy density, other requirements for the cathode material are high operating voltage, fast and reversible reactions with lithium ions, good ionic conductivity and reasonable electronic conductivity, stability with respect to cycling, and reasonably low volume change upon lithiation. In order to increase the energy density of batteries, research has lately focused on conversion cathodes.[9] Transition metal fluorides, especially, have been in focus thanks to their higher reaction potentials compared to metal oxide and metal sulfide conversion cathodes.

Whereas in the intercalation cathodes lithium ions are inserted in between the layered structure, with the conversion cathodes the whole operation principle is relying on chemical transformation. During the conversion, lithium ions bond to the anion, in this case fluoride, forming LiF. Simultaneously, metal ions are reduced to the metallic state and form nanodomains in the insulating LiF matrix. Equation 4 and Figure 15 describe the process.

(4) $x\,Li^+ + xe^- + MeF_x \leftrightarrow x\,LiF + Me$

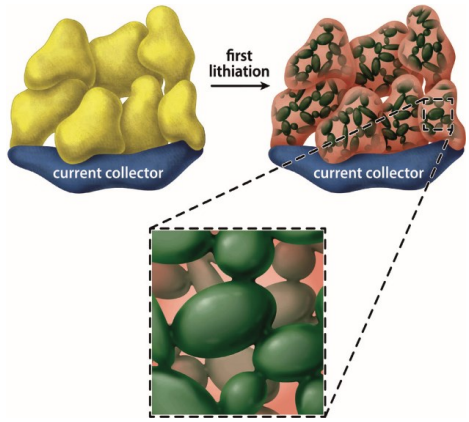

Figure 15 A schematic presentation of the conversion reaction between FeF_2 and Li^+. The yellow color depicts the FeF_2 material, the green color the iron nanodomains, and the red color the LiF matrix. Reprinted with permission from Ref. 60, Copyright 2011 American Chemical Society.

Whereas in the intercalation cathodes the lithium ions may occupy only certain sites, in the conversion cathodes all the transition metal sites are available for lithium ions. Thus, conversion cathodes have in general higher specific capacities than the intercalation cathodes. In addition, more than one Li^+ is needed in the reduction of the transition metal ion to the metallic state, which further increases the capacity. Specific capacities of several transition metal fluorides and a comparison of gravimetric energy densities between transition metal fluorides and some conventional intercalation cathode materials are presented in Figure 16. For comparison, the theoretical specific capacity of $LiCoO_2$ is ~270 mAh/g.[Ref. 61] In practice, however, the specific capacity is ~140 mAh/g, since not all the available sites are emptied from lithium ions.[61]

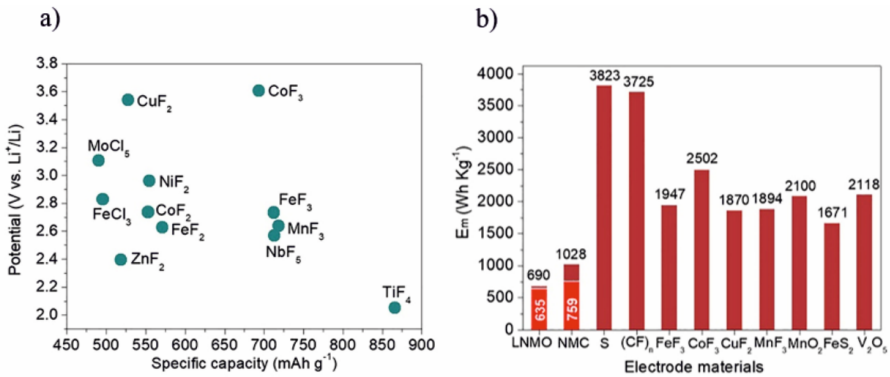

Figure 16 a) Specific capacities of several transition metal fluorides and b) comparison of gravimetric energy densities of some conventional intercalation cathode materials and transition metal fluorides. Reproduced with permission from Ref. 62, Copyright 2019 Elsevier.

Among the transition metal fluorides perhaps the best candidates for the conversion cathodes are iron fluorides that have large specific capacities and consist of abundant elements of low cost and low toxicity. Both FeF_2 and FeF_3 have been investigated as cathode materials for lithium-ion and sodium-ion batteries. In LIBs, FeF_2 has a gravimetric energy density of 1 519 Wh/kg and a specific capacity of 571 mAh/g.[Ref. 63] The reaction with Li ions is shown in Equation 5. [Ref. 60] The major concern regarding the use of FeF_2 is however the large volume change during the charging and discharging.

(5) $FeF_2 + 2e^- + 2\ Li^+ \rightarrow Fe + 2\ LiF$

FeF_3 has a specific capacity of 712 mAh/g and a gravimetric energy density of 1 951 Wh/kg with lithium.[63] In addition to conversion, FeF_3 has been shown to intercalate Li^+ ions thanks to the vacant octahedral interstices in the structure.[64] In FeF_3 nanocomposites the intercalation step is reversible, involving one electron as shown in Equation 6.[Ref. 65] In the conversion step, a two-electron reaction takes place (Eq. 7).[Ref. 66]

(6) $FeF_3 + Li^+ + e^- \rightarrow LiFeF_3$

(7) $LiFeF_3 + 2\ Li^+ + 2e^- \rightarrow 3\ LiF + Fe$

Also CoF_2 has been studied as a cathode candidate. CoF_2 has a specific capacity of 553 mAh/g and a gravimetric energy density of 1 578 Wh/kg with lithium.[63] It suffers from capacity decay, however.[67] It has been observed that after the delithiation, there is indeed still some LiF left.[67] The following reactions were proposed to take place during the battery operation:

(8) $CoF_2 + 2\ Li^+ + 2e^- \rightarrow Co + 2\ LiF$

(9) $x/2\ Co + LiF \leftrightarrow (1-x)\ LiF + x/2\ CoF_2 + x\ Li^+ + xe^-$

CoF_3 has been studied as well. However, it was observed that the reduction of Co^{3+} to metallic Co is not reversible.[68] Instead, during the reverse reaction CoF_2 is suggested to form. Therefore, the system would resemble the CoF_2/Li system discussed above. A drawback in the use of cobalt-based materials in general is the ethical issues still faced in cobalt mining. In addition, cobalt is not as abundant in the earth's crust as for example iron.

One issue common to all the transition metal fluoride cathodes is the poor electronic conductivity and hence fast capacity decay. Cathode dissolution has been observed too. One way to circumvent the poor electron conductivity is to embed the metal fluorides in a conducting matrix, for example, in amorphous carbon. This could also help to reduce the damage caused by the volume changes. Promising results were obtained when FeF_3 was combined with carbon nanofibers.[69] Also the electrolyte was chosen so that the cathode dissolution was suppressed. A reversible 500 mAh/g capacity was obtained during 400 cycles. An alternative strategy to improve the conductivity is to introduce additional anions in the structure, i.e., to form e.g. metal oxyfluorides.[9]

4 ATOMIC LAYER DEPOSITION

4.1 PRINCIPLE

Atomic Layer Deposition (ALD), originally known by the name Atomic Layer Epitaxy (ALE), was developed in Finland by Tuomo Suntola in the 1970's.[Ref. 70] A similar invention called Molecular Layering was independently made in The Soviet Union in the 60's.[Ref. 71,72] The motivation of Tuomo Suntola was to create a well-controlled thin film deposition method for flat panel electroluminescent displays.[72] The display technology development had been delayed due to insufficient quality of thin films deposited with the available methods of sputtering and vacuum evaporation. Atomic Layer Epitaxy was Suntola's solution to these issues.

The first material ever deposited by ALE was zinc sulfide that was then doped with manganese to be used as a luminescent layer in the displays. Although ALD had many outstanding properties, it did not yet become widely adopted, mainly due to its slowness. For many years, the applications of ALD were limited mostly to electroluminescent diplays.[72]

The real boom of ALD started in the late 90's when the semiconductor industry became interested in the technique. A deposition method was needed to realize the scale down of components and therefore to keep up with the Moore's law. The final breakthrough of ALD came with the hafnium oxide films used in gate oxides.[5] Ever since the 90's, the variety of applications of ALD has grown fast, now covering fields from, e.g., energy technologies to corrosion protection and medical technology. Despite the slow start, ALD is today considered as the most sophisticated and versatile thin film deposition method in many fields.

ALD is actually a variation of the chemical vapor deposition (CVD) method. The main difference between the traditional CVD and ALD is the precursor delivery. Whereas in CVD the precursors are fed into the reactor simultaneously and continuously and react in the gas phase or on the surface at high temperatures, ALD is based on sequential exposure of the substrate surface to the pulses of gaseous precursors (Fig. 17a).

The principle of ALD is presented in, e.g., a review article by Leskelä and Ritala.[1] An ALD process starts by introducing the first precursor in the chamber. This precursor chemisorbs or reacts with reactive sites, e.g., -OH groups, on the starting surface. The reaction continues until no -OH groups are left. After the pulse, an inert gas pulse purges away the unreacted precursor molecules as well as the side products formed in the reaction. Next, the second precursor is introduced, which then reacts with the species left on the surface in the first pulse. Again, the reaction continues until all the reactive sites have been used. Also after the second pulse, a purge follows. Because each reaction is saturated, the growth is said to be self-limiting. After the pulse-purge-pulse-

purge sequence – called as an ALD cycle – the original substrate surface has become covered with a monolayer (at maximum) of the material being grown. In practice, one ALD cycle is usually not enough to create a full monolayer of the material because the ligands in the precursor molecule block some of the reactive sites. This steric hindrance is illustrated in Figure 17b. Note, however, that despite the growth per cycle (GPC) is less than a monolayer, the growth is still self-limiting.

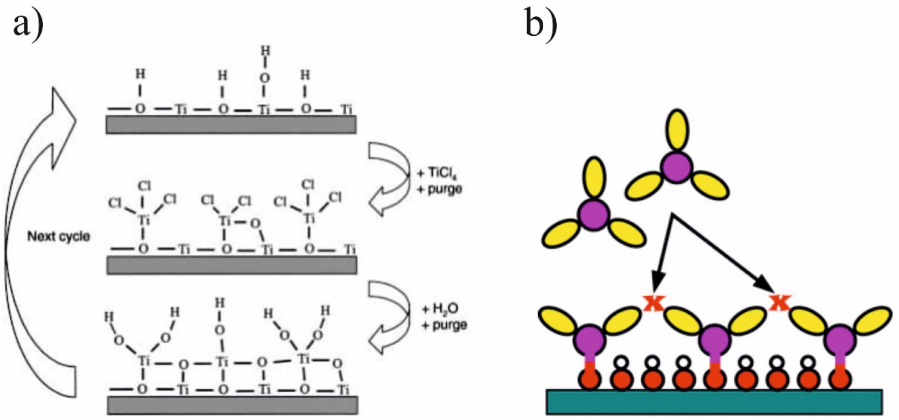

Figure 17 a) The principle of ALD and b) a schematical image of the steric hindrance caused by bulky ligands. a) Reproduced with permission from Ref. 1, Copyright 2003 John Wiley and Sons. b) Reproduced with permission from Ref. 73, Copyright 2016 American Chemical Society.

Due to the self-limiting reactions, ALD can produce stoichiometric and pure films with uniform and conformal coverage on the substrate surface. The ALD cycle is applied as many times as needed to produce a film with the desired thickness. ALD is in addition highly reproducible, i.e., in similar conditions (e.g. reactor set-up, temperature, precursor doses and pulse and purge times), films with the same thickness and properties are obtained.

The self-limiting nature of the method is straightforward to test and verify: as long as the purge time is sufficient, lengthening the precursor pulse times beyond certain points should not make the film thicker (Fig 18a). Likewise, the purge length can be lengthened without the GPC getting smaller. If, however, increasing the pulse length increases the GPC, the precursor might be decomposing. In turn, if the GPC decreases upon increasing the pulse time, the precursor might etch the film.

The growth temperature may have strong effect on the GPC, for example because of the thermodynamics and/or the density of reactive surface groups might be different. Self-limiting growth might still be encountered over a wide temperature range. In an ideal case, the GPC stays constant over a certain temperature range, i.e., a so-called ALD window is seen. The temperature range of self-limiting reactions might be limited at low temperatures by condensation or kinetics, and at high temperatures by precursor decomposition or desorption. Figure 18b illustrates these scenarios.

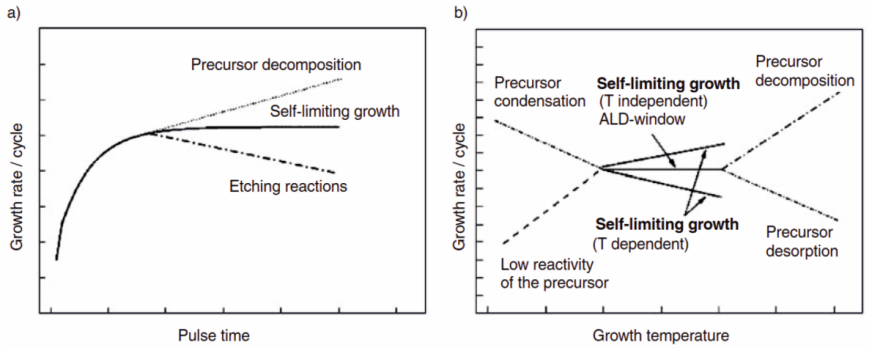

Figure 18 a) Effect of the pulse length and b) effect of the growth temperature on the growth per cycle. Reproduced with permission from Ref. 74 , Copyright 2008 Royal Society of Chemistry.

Due to the self-limiting growth mode, ALD is, opposite to e.g. PVD methods, suitable for conformal coating of complicated structures, such as nanoparticles, deep trenches, and curved surfaces. Compared to CVD, usually lower deposition temperatures are needed. With ALD, it is also possible to introduce dopants to the film with uniform distribution and sufficient separation by exploiting bulky ligands (Fig. 17b). ALD is thus an excellent method for introducing luminescent centers into films, which has inspired also this work.

Common reaction types in ALD include ligand-exchange reactions (Fig. 17a) and combustion reactions. In the ligand-exchange reactions, the first precursor, e.g., $TiCl_4$, is reacting with the active sites of the substrate surface leaving $TiCl_x$ species on the surface. The next precursor, e.g., H_2O, then reacts with these surface groups forming Ti-O bonds. The chloride ions originally attached to titanium combine with the hydrogen ions of the water molecules. Ligand exchange reactions are common for example in metal oxide, sulfide, nitride, and fluoride deposition. A metathesis reaction in Eq. 10 describes the overall reaction:

(10) $AX + BY \rightarrow AY + BX$

The other common reaction in ALD is combustion. After the metal precursor pulse and purge, the organic ligands of the precursor are combusted by, e.g., an ozone pulse or oxygen plasma. The combustion byproducts are, e.g., CO_2 and H_2O. The final film composition depends on the favorability (thermodynamics and kinetics) of the reactions between the metal cation introduced in the first pulse and the different combustion products. For example, the reaction of $Fe(thd)_3 + O_3$ results in iron oxide deposition whereas in the reaction of Lithd + O_3, a lithium carbonate film is formed.

4.2 PRECURSORS IN ATOMIC LAYER DEPOSITION

An ideal ALD precursor should have the following properties: good volatility to ensure efficient transportation to the substrate, aggressive reactions with the other precursors, and thermal stability within the deposition temperature range. In addition, the precursors should preferably be in the liquid or gas form because of their easy and consistent delivery. Other properties good to have include non-toxicity, easy handling, stability in air, and low price. Side products formed in the reactions should be non-reactive and volatile to allow their easy removal from the reactor during the purge. Chemically benign side products are an asset. In reality, few precursors meet all the properties mentioned here. Often compromises must be made.

Common metal precursors include halides, alkoxides, β-diketonates, alkyls, cyclopentadienyls, amides, and amidinates. For some metals, the vapor pressure of the elemental form allows its use as such.[70,75–77] Some of these precursor types are summarized in Figure 19. The common and important β-diketonate ligand 2,2,6,6-tetramethyl-3,5-heptanedione (thd) is shown in Figure 19c. Widely used non-metal precursors include hydride compounds (e.g. H_2O, H_2S, and NH_3) for the ligand exchange type reactions, but in the case of sulfur, selenium and tellurium also the elemental form can be used.[70,78,79] For the metal precursor combustion, O_3 and O_2 have been used. O_2 usually needs activation by plasma, however. In ALD of noble metals, the film itself can catalytically activate O_2 by dissociating it to atomic oxygen.[80]

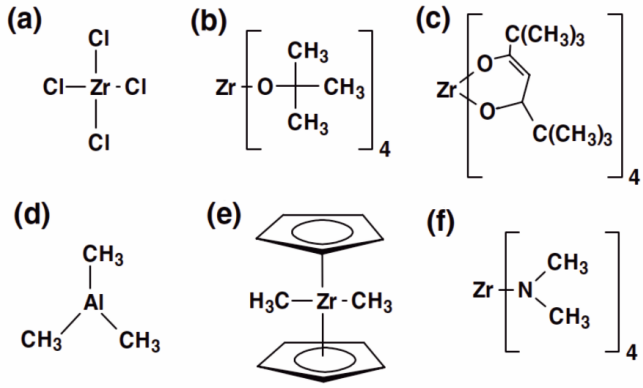

Figure 19 Common metal precursors in ALD include a) halides, b) alkoxides, c) β-diketonates, d) alkyls, c) cyclopentadienyls and d) amides. The ligand in c) is bis(2,2,6,6-tetramethyl-3,5-heptanedionato), e.g., thd. Reprinted with permission from Ref. 81, Copyright 2004 John Wiley and Sons.

4.3 ATOMIC LAYER DEPOSITION OF METAL FLUORIDES

One of the main issues in depositing metal fluorides with ALD has been the lack of good fluoride precursors. The most obvious fluoride source would be hydrogen fluoride, being analogous to water, ammonia, and hydrogen sulfide. However, HF is highly toxic and etches metals and glass. It is therefore seldom used as a precursor as such.[82–84] Instead, HF has been mixed with pyridine to produce a safer-to-handle liquid precursor called Olah's reagent. Some transition metal fluorides, for example, were deposited by Lee at al. using this precursor.[85]

HF has also been produced *in situ* in an ALD reactor.[86] Solid NH_4F decomposes upon evaporation into HF and NH_3. Despite producing good quality films, the downside of NH_4F is that HF forming inside the reactor can still damage glass and metal parts of the reactor and the pump. Another nuisance is the NH_3 formed in the decomposition. Depending on the material to be grown, a competing metal nitride formation might interfere with the metal fluoride growth. NH_4F has been used for the deposition of e.g., CaF_2 and ZnF_2.[Ref. 86] The metal precursors were $M(thd)_x$ and acetate for zinc. It has also been reported that $ZnCl_2$ and $AlCl_3$ were not producing films with NH_4F.[86]

Metal fluorides (TiF_4 and TaF_5) were presented as more benign fluoride precursors by Pilvi et al.[87–91] The growth proceeds with a ligand exchange reaction with $M(thd)_x$, where volatile $Ti(thd)_4$ or $Ta(thd)_5$ or their partially fluorinated versions are produced as side products. Later also $AlCl_3$ was used with TiF_4 to deposit AlF_3[Ref. 92]. Usually, a strong decrease in GPC is seen along the increasing deposition temperature. Decreasing density of TiF_x groups on the surface has been proposed as the reason. At low deposition temperatures,

extreme GPC values are seen, e.g., ~5 Å for LaF_3 at 250 °C.[Ref. 90] It has been proposed that a monolayer of film material would form during both precursor pulses. Thus far, the growth mechanism has been resolved only for AlF_3.[Ref.93] It was revealed that during the TiF_4 pulse TiF_4 first reacts with aluminum chloride species on the surface to form AlF_3, and then TiF_4 adsorbs molecularly on top of the AlF_3 layer. During the $AlCl_3$ pulse, however, no molecular $AlCl_3$ adsorption seems to take place.

The more benign precursors TiF_4 and TaF_5 have drawbacks, however. The films often contain titanium or tantalum impurities that increase the absorption of light at the UV wavelengths. Therefore, these processes have not completely fulfilled the requirements of optical applications. After the introduction of TiF_4 and TaF_5, also WF_6 has been reported in combination with trimethylaluminum (TMA).[94] However, in this case remarkable amounts of metallic tungsten and tungsten carbide were present in the AlF_3 films.

A different approach to the fluoride deposition was presented by Putkonen et al.[95] They used ozone to combust fluorinated ligands (hexafluoroacetylacetonate, hfac). Two ways for depositing CaF_2 films were presented. In the first approach, $Ca(hfac)_2$ was used as a precursor together with ozone. The process is similar to the ozone-based oxide and carbonate formation. First, $Ca(hfac)_2$ is pulsed and chemisorbed on the substrate. The subsequent ozone pulse then combusts the organic ligands, and from the combustion products calcium ions bond with fluoride and CaF_2 is formed. The second approach involves $Ca(thd)_2$, ozone and free Hhfac ligand. The first part of the cycle follows a typical sequence of a metal thd + ozone process: once the substrate surface has been saturated with $Ca(thd)_2$ molecules, the ozone pulse combusts the ligands and $CaCO_3$ is formed. In the fluoride process the cycle is continued with Hhfac and O_3 pulses, leading to the formation of CaF_2. The second approach was applied also in the deposition of MgF_2 and LaF_3.

Given that both approaches involve combustion of the ligands, impurities could be expected to be an issue. In the first approach, the amount of oxygen in the CaF_2 films was < 5 at%, as measured by Rutherford backscattering spectrometry (RBS). In the second approach, the oxygen contents of the CaF_2 and LaF_3 films were < 2 at%, i.e., lower than the detection limit of RBS. Also the stoichiometry of the films was better.

In addition to thermal ALD, metal fluorides have been deposited with plasma ALD; LiF and AlF_3 were deposited using SF_6 plasma as the fluoride source and lithium bis(trimethylsilyl)amide ($LiN(SiMe_3)_2$) and TMA as the metal precursors.[96,97] AlF_3 has been deposited also by exposing ALD-made Al_2O_3 films to CF_4 plasma.[98]

Most of the published ALD processes are for binary fluorides. Of ternary fluorides, only $LiAl_xF_y$, AlO_xF_y, ZnO_xF_y, ZrO_xF_y and HfO_xF_y have been reported.[99–103] AlO_xF_y was obtained by combining TMA, H_2O and HF pulses.[101] Also the deposition of Al_2O_3 and AlF_3 laminate structure resulted in AlO_xF_y films. Similar approaches were used for deposition of ZrO_xF_y and HfO_xF_y.[103] Lithium aluminum fluoride was obtained by combining LiO^tBu, $AlCl_3$ and TiF_4

or by exposing AlF_3 films to Lithd vapor.[99,100] ZnO_xF_y films were obtained by combining $ZnEt_2$ and aqueous solution of HF.[Ref. 102]

Table 1 summarizes the ALD processes of metal fluorides. The processes that were developed during this work are not included.

Table 1. *Published ALD processes for metal fluorides.*

Material	Precursors	Deposition temperature	Reference
LiF	Lithd + TiF_4	250–350 °C	104
	LiO^tBu + TiF_4	200–300 °C, 220 °C	100,105
	LiO^tBu + HF/pyridine	150 °C	106
	LiO^tBu + NH_4F	150–300 °C	107
	LiO^tBu +Hhfac	220 °C	105
	$LiN(SiMe_3)_2$ + HF	100–250 °C	82
	$LiN(SiMe_3)_2$ + HF/pyridine	125–250 °C	108
	$LiN(SiMe_3)_2$ + SF_6 plasma	150 °C	96
	MgF_2 + TiF_4 + Lithd + TiF_4	275–350 °C	109
	MgF_2 + Lithd	325 °C	109
NaF	NaO^tBu + HF/pyridine	175–250 °C	110
MgF_2	$Mg(thd)_2$ + TiF_4	250–400 °C	87
	$Mg(thd)_2$ + TaF_5	225–400 °C	91
	$Mg(thd)_2$ + O_3 + Hhfac + O_3	250–350 °C	95
	$Mg(EtCp)_2$ + HF	100–250 °C	83
	$Mg(EtCp)_2$ + HF/pyridine	150 °C	85
AlF_3	$AlCl_3$ + TiF_4	160–340 °C	92
	$AlMe_3$ + HF/pyridine	75–250 °C, 155–200 °C	111,112
	$AlMe_3$ + TaF_5	125 °C	113
	$Al(NMe_2)_3$ + HF	125–162 °C	84
	$AlMe_3$ + SF_6 plasma	50–300 °C	97
	Al_2O_3 + CF_4 plasma	300 °C	98
CaF_2	$Ca(thd)_2$ + TiF_4	300–450 °C	88

	$Ca(thd)_2 + NH_4F$	300–400 °C	86
	$Ca(hfac)_2 + O_3$	300 °C	95
	$Ca(thd)_2 + O_3 + Hhfac + O_3$	250–350 °C	95
MnF_2	$Mn(EtCp)_2 + HF/pyridine$	150 °C	85
ZnF_2	$Zn(OAc)_2 + NH_4F$	260–320 °C	86
	$ZnEt_2 + HF/pyridine$	150 °C	85
SrF_2	$Sr(thd)_2 + NH_4F$	260–320 °C	86
YF_3	$Y(thd)_3 + TiF_4$	175–325 °C	89
ZrF_4	$Zr(O^tBu)_4 + HF/pyridine$	150 °C	85
	$Zr(NEtMe)_4 + HF/pyridine$	150 °C	85
LaF_3	$La(thd)_3 + TiF_4$	225–350 °C	90
	$La(thd)_3 + O_3 + Hhfac + O_3$	250–350 °C	95
SmF_3	$Sm(thd)_3 + NH_4F$	250 °C	114
EuF_3	$Eu(thd)_3 + NH_4F$	250 °C	114
TbF_3	$Tb(thd)_3 + NH_4F$	250 °C	114
HfF_4	$Hf(NEtMe)_4 + HF/pyridine$	150 °C	85
$LiAl_xF_y$	$LiO^tBu + AlCl_3 + TiF_4$	250 °C	100
	$AlF_3 + Lithd$	250–300 °C	99
AlO_xF_y	$AlMe_3 + H_2O + HF/pyridine$	150 °C	101
ZnO_xF_y	$ZnEt_2 + H_2O/HF$	140 °C	102
ZrO_xF_y	$Zr(NEtMe)_4 + H_2O + HF/pyridine$	150 °C	103
HfO_xF_y	$Hf(NMe_2)_4 + H_2O + HF/pyridine$	150 °C	103

5 EXPERIMENTAL

5.1 FILM DEPOSITION

All the depositions were done in an ASM F120 cross-flow reactor. The working pressure in the reactor was around 5–10 mbar. Nitrogen (99.999%) served as the carrier and purging gas. Most of the depositions were done on Si substrates with the native oxide. Sapphire, graphite, and indium tin oxide (ITO) coated glass were used for special purposes.

Mostly thd compounds were used as metal precursors. They are well studied in ALD literature in general as well as in ALD metal fluoride processes. They are easily available for rare earth metals at a reasonable price. For cobalt (II) fluoride deposition with NH_4F, $CoCl_2$TMEDA was used, since no film growth was observed with the $Co(thd)_2$ + TiF_4 and $Co(thd)_2$ + NH_4F combinations.

TiF_4, TaF_5, NH_4F, and NbF_5 were used as the fluoride source. TiF_4 is known to work well with metal thd compounds, as described in section 4.3. NH_4F in turn is the best precursor choice when metal fluorides cannot be used as precursors. On one hand, this involves precursors that do not have suitable thermodynamics to react with metal fluorides. On the other hand, if the film is deposited for UV applications, it might be better to avoid using metal fluorides precursors that incorporate UV-absorbing impurities into the films. NbF_5 is presented here as a new fluoride precursor. Previously, NbF_5 has been used in ALD as a niobium source.[115]

5.2 FILM CHARACTERIZATION

Only an overview of the characterization methods is provided here. Details are found in the articles I–IV.

The thicknesses and refractive indices of the films were measured with an ellipsometer. In some cases, x-ray reflection (XRR), UV-Vis spectrometry, and cross-section scanning electron microscopy were used for the thickness measurement.

Grazing incidence x-ray diffraction (GI-XRD) was used for studying the crystallinity of the films. The crystalline phases were identified with a High Score software. High temperature x-ray diffraction (HTXRD) was used to investigate changes in crystal structure and lattice parameters during heating of the sample.

The elemental compositions and depth distributions of the elements were studied with Time-of-Flight Elastic Recoil Detection Analysis (ToF-ERDA). EDS was used to qualitatively study the film composition. Because the light element fluorine is the other main constituent of the films, quantitative EDS measurements are not trivial and typically too high atomic concentrations are measured for fluorine. Therefore, EDS measurement are in most cases used only to support the ToF-ERDA results.

The morphology of the films was studied with field emission scanning electron microscopy (FESEM). The morphology and roughness of the most interesting films were further studied with atomic force microscopy (AFM).

Dielectric measurements of GdF_3 films as a part of capacitor were done with LCR meter. I-V measurements were performed as well.

6 RESULTS AND DISCUSSION

6.1 TERBIUM FLUORIDE

Article I describes an ALD process for TbF_3. The study was motivated by Tb^{3+} being a widely used green light emitter in luminescence devices. The choice of the counter ion, fluoride, stems from the compatibility with host structures which in many interesting cases are rare earth metal fluorides. In the previous works by Pilvi et al., rare earth fluorides have been deposited by ALD using rare earth thd compounds and titanium fluoride as precursors.[87–90] This was the starting point for the current study as well.

In general, the combination of $Tb(thd)_3$ and TiF_4 produces uniform films at the studied deposition temperature range of 175–350 °C. According to XRD, the films consist of the orthorhombic TbF_3. The film deposited at 175 °C is only weakly crystalline, however. The saturation of the GPC with respect to pulses and purges was studied at 300 °C. Unlike in several previous TiF_4-based ALD processes, the GPC saturates nicely, resulting in a GPC of 0.7 Å as seen in Figure 20.

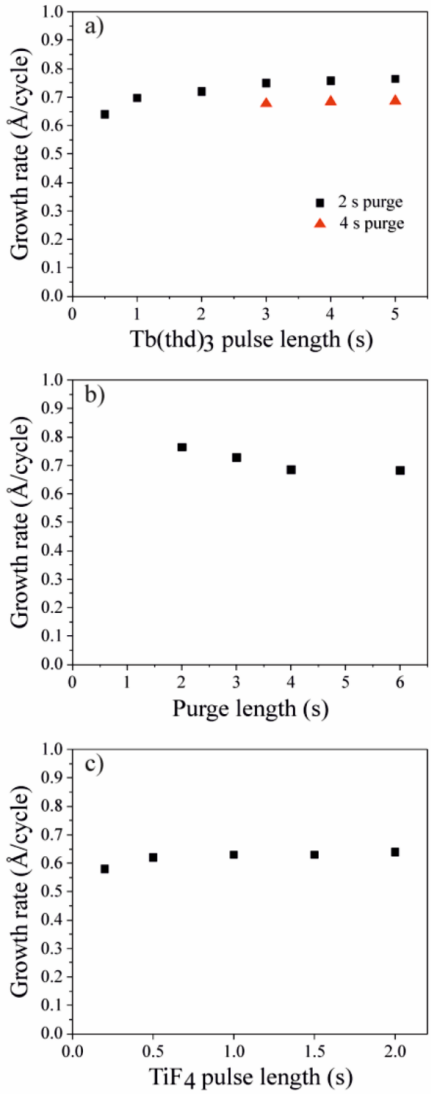

Figure 20 GPC as a function of (a) $Tb(thd)_3$ pulse length, (b) purge length and c) TiF_4 pulse length. Reproduced with permission from article I, Copyright 2021 American Vacuum Society.

At other deposition temperatures, the GPC is 0.5–1.5 Å (Fig. 21). It is lower compared to other ALD metal fluoride processes using TiF_4 as the fluoride precursor. The reason for the lower GPC of TbF_3 is not known, and further mechanism studies would be needed. However, the role of thermodynamics was evaluated by calculating Gibbs free energy changes for several ALD metal fluoride processes. The calculations were done by approximating the metal-thd bonds with metal-oxide bonds. All the calculated Gibbs free energy

changes lie in the range of -261 to -139 kJ/mol (Table 2). The ΔG for TbF_3 (-231 kJ/mol) does not deviate from the other values. It is assumed, therefore, that thermodynamics is not the reason for the different GPC. Despite the lower GPC of the TbF_3 process, the trend in the GPC along the increasing temperature is similar to the other processes. The GPC decreases strongly when the deposition temperature is increased.

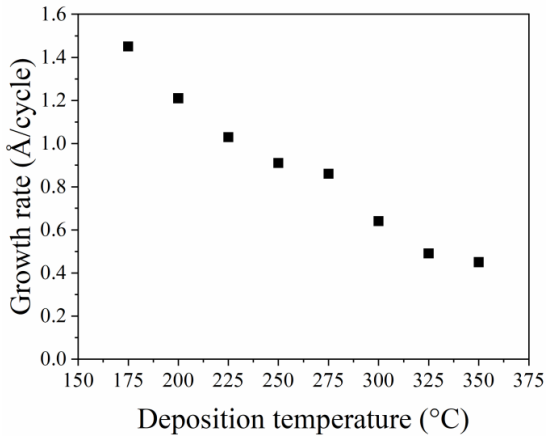

Figure 21 GPC of TbF_3 at different deposition temperatures. Reproduced with permission from article I, Copyright 2021 American Vacuum Society.

Table 2. *Calculated Gibbs free energy changes for the formation of metal fluorides from $M(thd)_x$ + TiF_4 at 300 °C using metal oxides as an approximation for the metal-thd complexes.*

Example reaction: 2 Tb_2O_3 + 3 TiF_4 → 4 TbF_3 + 3 TiO_2	
Material	Calculated ΔG (kJ/mol)
LaF_3	-261
CaF_2	-234
TbF_3	-231
YF_3	-230
MgF_2	-163
LiF	-139

In the previous ALD studies using TiF_4 as the fluoride source, Ti impurities in the films have been an issue. In the TbF_3 process, the films deposited at 175–225 °C have Ti contents between 2.5–3.7 at-%, decreasing with increasing deposition temperature (Table 3). At 275–350 °C the films turned out to have low titanium contents, if any, as measured by ToF-ERDA (detection limit of 0.1 at-%). Also, EDS measurements could not detect titanium in these films. One possible explanation for the low titanium contents in the TbF_3 films is that

the lower GPC, as compared to other TiF_4-based processes, allows the ligand exchange reactions to proceed closer to the completion. During the ToF-ERDA-measurements, the films eroded fast, and therefore no reliable depth profiles were obtained.

Table 3. *Elemental composition and stoichiometry of approximately 100 nm films measured by ToF-ERDA*

T_{dep} (°C)	Tb (at-%)	F (at-%)	H (at-%)	C (at-%)	O (at-%)	Ti (at-%)	F/Tb
175	17.8 ± 0.3	62.7 ± 1.2	5.9 ± 1.5	4.3 ± 0.3	5.6 ± 0.4	3.7 ± 0.2	3.5
200	18.3 ± 0.2	61.4 ± 0.8	7.2 ± 1.2	5.3 ± 0.2	5.1 ± 0.2	2.64 ± 0.13	3.4
225	18.5 ± 0.2	62.3 ± 0.7	7.8 ± 1.2	4.3 ± 0.2	4.5 ± 0.2	2.47 ± 0.12	3.4
275	24.32 ± 0.14	73.0 ± 1.0	0.8 ± 0.3	0.24 ± 0.04	1.68 ± 0.15	-	3.0
300	25.27 ± 0.15	72.7 ± 1.0	0.3 ± 0.2	0.9 ± 0.2	0.89 ± 0.11	-	2.9
350	24.36 ± 0.15	73.0 ± 1.1	1.0 ± 0.7	0.93 ± 0.14	0.72 ± 0.08	-	3.0

Literature on synthesis of TbF_3 in thin film form is scarce. Paramasivam et al. prepared TbF_3 as a part of a capacitor structure by thermal evaporation method.[116] The study concentrated on the electrical properties of the film and very little details on the film quality were given. Another report on TbF_3 thin films is found in the dissertation by L. J. Lingg.[117] TbF_3 films were deposited by thermal evaporation at room temperature and at 200 °C. In both cases, the F/Tb ratio was very close to 3 (2.95 and 2.99) as measured by RBS. The oxygen content was 4.5 at-% in the film deposited at room temperature, but in the film deposited at 200 °C no oxygen was detected. The films deposited at room temperature were x-ray amorphous whereas the films deposited at 200 °C were polycrystalline and consisted of the orthorhombic TbF_3 like the films deposited with the current process. Yet one more article reports using ALD for TbF_3 deposition. Hansen et al. used $Tb(thd)_3$ and NH_4F to deposit TbF_3 as a part of an organic-inorganic nanocomposite.[114]

Although the process developed in the current work is a film consisting of only TbF_3, the same deposition process is likely to work also as a part of a host/luminescent center structure, i.e., GdF_3/TbF_3. With ALD, the uniform distribution of TbF_3 in GdF_3 host can be obtained.

6.2 GADOLINIUM FLUORIDE

Gadolinium fluoride is one of the rare earth fluorides that are interesting host structures for the luminescent centers. ALD of GdF_3 was studied in article II. The most obvious choice for the ALD process would be the combination of $Gd(thd)_3$ + TiF_4, similar to TbF_3. However, as GdF_3 thin films have applications also as UV-antireflective coatings, it was desirable to replace TiF_4 with a fluoride source that is not leaving absorbing impurities in the films. HF was therefore chosen as the fluoride source. HF was generated *in situ* by decomposing NH_4F into HF and NH_3 by annealing.

The film growth was studied at 275–375 °C using $Gd(thd)_3$ as the gadolinium source. Crystalline, orthorhombic films were obtained at all the deposition temperatures. At 275 °C, an additional XRD reflection, possibly belonging to Gd_2O_3, was seen. Therefore, no depositions were done below 275 °C.

The films deposited at 285–375 °C looked uniform to the eye. According to ToF-ERDA, the F/Gd ratio varied between 2.7 and 3.3, and the impurity contents were low. Most importantly, the nitrogen content was less than 0.1 at-% in all the films. In the films deposited at 300 and 325 °C, no nitrogen was detected with ToF-ERDA. The low nitrogen content is a clear indication that NH_3, that is forming upon the NH_4F decomposition, is not interfering with the GdF_3 growth.

Unlike in the ALD processes that use TiF_4 as the fluoride precursor, the GPC of this process is only weakly dependent on the deposition temperature (Fig. 22). In fact, whereas in the TiF_4-based processes the growth per cycle decreases strongly as the deposition temperature increases, in this process the growth per cycle increases, though only slightly. Therefore, the process is more tolerant to possible deposition temperature fluctuations.

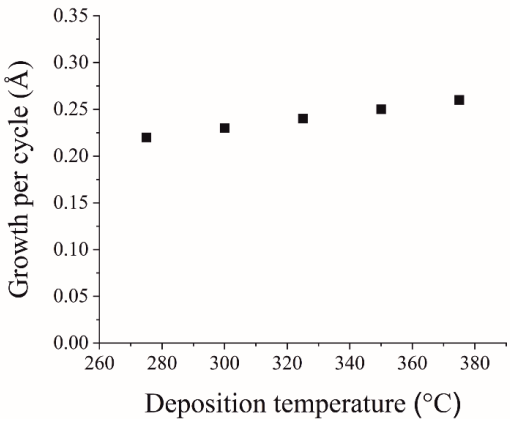

Figure 22 The growth per cycle values of GdF_3 at different deposition temperatures. Reproduced with permission from article II, Copyright 2022 American Vacuum Society.

In antireflection coatings the films should be as smooth as possible to avoid scattering losses. Like many other metal fluoride films grown by ALD, these GdF_3 films were quite rough, however. In addition, a special trend in the film growth was observed in FESEM. For the films deposited at 300–375 °C, the surface becomes more homogenous as the deposition temperature is increased (Fig. 23). Therefore, the film deposited at 300 °C is the roughest. The root mean square roughness (R_q) values of the films deposited at 300, 325, 350, and 375 °C are 9.5, 6.5, 6.3, and 8.1 nm, respectively (Fig. 24). These films were about 100 nm in thickness.

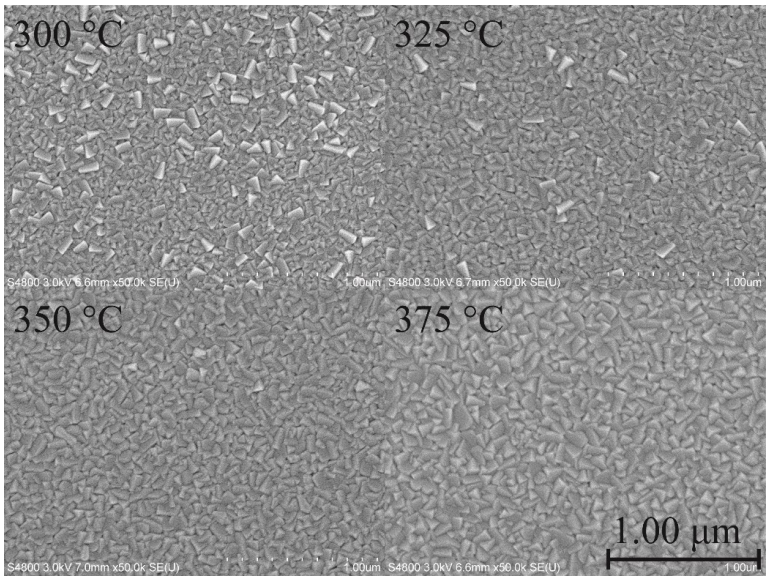

Figure 23 FESEM images of GdF_3 films deposited at 300–375 °C. Reproduced with permission from article II, Copyright 2022 American Vacuum Society.

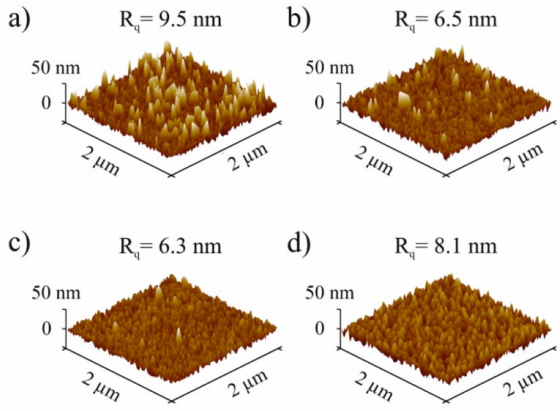

Figure 24 AFM images and roughnesses of GdF_3 films deposited at a) 300, b) 325, c) 350 and d) 375 °C. Reproduced with permission from article II, Copyright 2022 American Vacuum Society.

The antireflection properties of the GdF_3 films were studied by UV-Vis transmittance. Figure 25 shows the UV-Vis transmission spectra of a bare sapphire substrate and a GdF_3-coated sapphire. As expected, the transmission of the GdF_3/sapphire system is higher over the whole wavelength range as compared to the bare sapphire. A refractive index of 1.50–1.51 was determined for the GdF_3 film. Evaluating the applicability of the GdF_3 ALD process for real antireflection coatings could be studied as well, for example by depositing MgF_2 and GdF_3 layers on a CaF_2 substrate. The biggest concern is however the roughness of the ALD films.

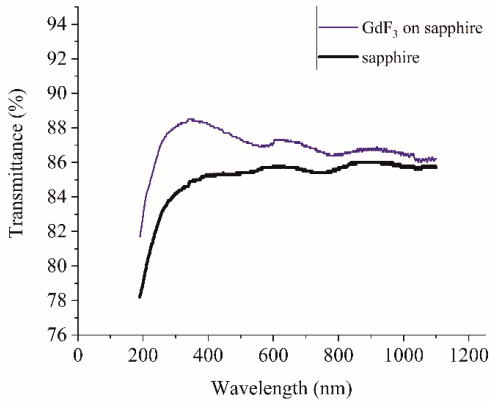

Figure 25 UV-Vis transmission spectra of a GdF_3 film deposited on a sapphire substrate at 300 °C and a bare sapphire substrate.

In the studies on ALD of cesium fluoride (section 6.8.2) we noticed that NH_4F as the fluoride source might cause Si incorporation into the films. The Si content of a GdF_3 film was therefore measured with ToF-ERDA. Since the fast erosion of the films makes the depth profiling troublesome, as discussed in the TbF_3 section, the GdF_3 film was capped with a Ta_2O_5 layer. The erosion was much slower, and the Si signals originating from the film and from the substrate could be separated. There was indeed a small Si content in the bulk of the GdF_3 film. However, the Si content was only 0.19 at-%.

In the literature, deposition of GdF_3 films with thermal evaporation has been reported.[117–123] No CVD processes exist to our knowledge. Most of the studies concentrate on the optical and mechanical properties of the films. In general, quite thick films have been deposited, resulting in orthorhombic polycrystalline films at high deposition temperatures and amorphous films at room temperature. With respect to the current study, the most relevant comparison is the work by Jin et al. where 27 nm GdF_3 films were thermally evaporated on fused silica substrates.[119] According to XRD, the films were crystalline at 150–380 °C substrate temperatures. The rms roughness of the films was remarkably lower than of our films: 0.7 to ~1.0 nm according to AFM. The highest roughnesses were measured from the films deposited at the lowest temperatures, which is in line with the result from the current study.

6.3 SODIUM GADOLINIUM FLUORIDE

Once a successful process for GdF_3 was developed, deposition of $NaGdF_4$ was attempted. $NaGdF_4$ is an interesting host material for luminescent centers and was therefore included in this work.

First, $NaGdF_4$ deposition by the conventional supercycle ALD approach, i.e., by combining $Gd(thd)_3/NH_4F$ and $Nathd/NH_4F$ binary cycles, was attempted. NaF deposition by the Nathd + NH_4F process was successfully tested in advance. GdF_3 and NaF cycles were sequentially supplied on Si substrates at 300 °C. The GdF_3/NaF cycle ratio was varied from 2:2 to 8:2, i.e., one supercycle consisted of 2 to 8 cycles of GdF_3 and 2 cycles of NaF. The films were characterized with XRD. The as-deposited films with cycle ratios from 2:2 to 7:2 consisted of both the hexagonal $NaGdF_4$ and the cubic NaF (Fig. 26). When the cycle ratio was 8:2, the NaF phase was barely detectable. However, it was noticed that the films deposited with cycle ratios higher than 5:2 were either blur looking, almost powder like, or reacted immediately when exposed to air. The reason for this behavior is unclear. In the previous ALD studies involving sodium it has been noted that sodium might destroy the ALD-type growth by diffusing in the films and reacting to hydroxides upon contact with water.[124,125]

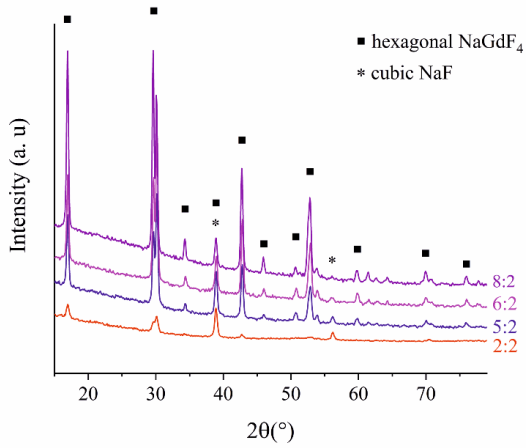

Figure 26 GI-x-ray diffractograms of films deposited with various GdF_3/NaF pulsing ratios at 300 °C.

To overcome the issues encountered with the supercycle approach, GdF_3 films were converted to $NaGdF_4$ by exposing them to Nathd vapor inside the ALD reactor at elevated temperatures. Similar methods have been previously reported for lithiation of thin films, such as converting AlF_3 to Li_3AlF_6 as well as converting MgF_2 films to LiF films.[99,109] The starting GdF_3 films were approximately 26 nm thick, and different numbers of Nathd pulses were applied at 300 °C. After exposure to the Nathd vapor, the films were visibly unchanged, and no blurring occurred. According to XRD, the GdF_3 films exposed to 1000 and 1500 pulses of Nathd consisted of the hexagonal $NaGdF_4$ and orthorhombic GdF_3 (Fig. 27). In the 1500 Nathd pulse film, the GdF_3 component was hardly detectable, however.

The completeness of the conversion reaction is hard to analyze. Depth profiling by ToF-ERDA could be attempted, but the fast erosion of many ALD metal fluoride films makes the results unreliable. Capping of metal fluoride films has been shown to hinder the erosion. However, the diffusion of Na^+ ions during the capping layer deposition could be an issue. HTXRD combined with high temperature x-ray reflection (HTXRR) would be another option to study the completion of the $NaGdF_4$ formation. The combination of HTXRD and HTXRR has been previously used by our group to study the conversion of selected metal oxides to corresponding lithium or sodium metal oxides.[126]

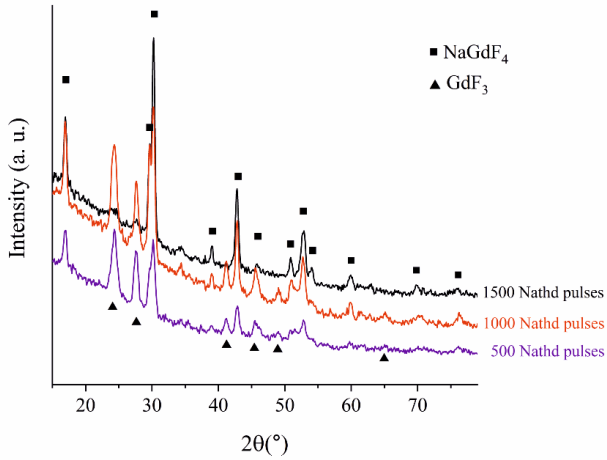

Figure 27 GI-x-ray diffractograms of GdF_3 films exposed to various number of Nathd vapor pulses at 300 °C.

6.4 COBALT(II) FLUORIDE

The motivation for depositing CoF_2 by ALD comes from its use as a lithium-ion battery cathode. Of the potential transition metal fluoride LIB cathode materials (FeF_2, FeF_3, CoF_2, CoF_3, NiF_2 and CuF_2) CoF_2 is the first one for which an ALD process is reported.[III]

In the studies on ALD of FeF_3, several precursor combinations were studied (section 6.8.1). The best results were obtained with the combination of $FeCl_3$ and NH_4F. Although no ALD-like growth was observed in this process, it gave an idea to test cobalt chloride as a precursor for the CoF_2 deposition. $CoCl_2$ is however unsuitable for ALD due to its low vapor pressure. A more volatile version of $CoCl_2$ was introduced in the work by Väyrynen et al.[127] This precursor is $CoCl_2$(TMEDA), which has an additional neutral adduct ligand of TMEDA (TMEDA = N,N,N′,N′-tetramethylethylenediamine). In ALD processes, upon the chemisorption of $CoCl_2$(TMEDA), the adduct ligand is thought to detach and the reacting species is cobalt chloride. We adopted this precursor to the CoF_2 process.

Deposition of CoF_2 from $CoCl_2$(TMEDA) and NH_4F was tested at 180–275 °C. The evaporation temperature of $CoCl_2$(TMEDA) was 175 °C and it has been reported to decompose at 300 °C. The saturation of the GPC as a function of the $CoCl_2$(TMEDA) and NH_4F pulse times was studied and achieved at 250 °C resulting in a GPC of around 1 Å. The films deposited at 180–275 °C are crystalline and contain tetragonal CoF_2 according to XRD. The stoichiometry and impurity contents were measured with ToF-ERDA (Table 4). The stoichiometry of the films is in accordance with the XRD results. The impurity contents are low, especially in the films deposited at temperatures higher than

200 °C. In a film deposited at 250 °C, for example, the sum of the H, C, N, O, and Cl contents is only 1.15 at-%. The low N and Cl contents (0.04 and 0.13 at-%) indicate that the precursor combination of the cobalt chloride adduct and ammonium fluoride is working well. To our knowledge, metal chloride and ammonium fluoride combination has not been used successfully in ALD before.

Table 4. *Elemental composition and stoichiometry of CoF_2 films deposited with 1000 cycles as measured by ToF-ERDA*

	T_{dep} 180 °C	T_{dep} 200 °C	T_{dep} 225 °C	T_{dep} 250 °C	T_{dep} 275 °C
Co (at-%)	33 ± 2	31.64 ± 1.00	32.6 ± 0.8	31.2 ± 0.6	33.36 ± 0.62
F (at-%)	61 ± 5	63 ± 2	65 ± 2	68 ± 2	64.07 ± 1.28
H (at-%)	2.1 ± 0.9	3 ± 2	0.9 ± 0.3	0.25 ± 0.08	0.76 ± 0.25
C (at-%)	0.62 ± 0.12	1.1 ± 0.3	0.60 ± 0.15	0.10 ± 0.01	0.68 ± 0.25
N (at-%)	0.11 ± 0.01	0.19 ± 0.08	0.04 ± 0.00	0.04 ± 0.00	0.03 ± 0.00
O (at-%)	2.3 ± 0.2	0.98 ± 0.06	0.79 ± 0.06	0.63 ± 0.04	0.92 ± 0.06
Cl (at-%)	0.60 ± 0.08	0.28 ± 0.07	0.23 ± 0.05	0.13 ± 0.02	0.17 ± 0.03
F/Co	1.8	2.0	2.0	2.2	1.9

The morphology of the films is strongly dependent on the deposition temperature as seen in the FESEM images (Fig. 28). The films deposited at lower temperatures consist of rod-like grains pointing to different directions whereas in the films deposited at higher temperatures cubic-like shapes are seen. The films deposited at higher temperatures also look smoother.

As mentioned earlier, roughnesses of metal fluoride films deposited by ALD are often remarkable. In the case of CoF_2 the roughness is extremely large for the films deposited at lower temperatures. As an example, for a 69 nm film deposited at 200 °C the roughness is ~25 nm (Fig. 28). As a comparison, the roughnesses of approximately 100 nm GdF_3 films varied between 6.3 and 9.5 nm.

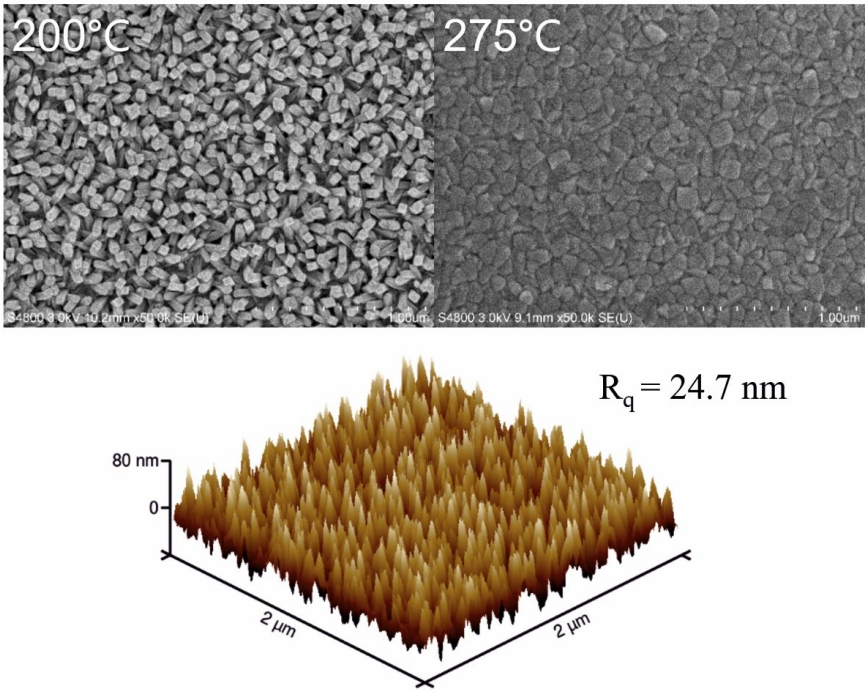

Figure 28 FESEM image of CoF_2 films deposited with 1000 cycles at 200 and 275 °C and an AFM image of a 69 nm CoF_2 film deposited at 200 °C. Reproduced and adapted with permission from article III. Copyright 2023 Authors. Distributed under a Creative Commons Attribution (CC BY 3.0) License.

For the battery applications, the poor electronic conductivity of metal fluoride cathodes has been compensated by combining them with conducting materials, such as carbon.[69] CoF_2 film growth was therefore briefly studied also on a graphite substrate. At 250 °C tetragonal CoF_2 was obtained (Fig. 29). With FESEM, similar rod-like grains were seen as in the films grown on silicon substrates (Fig. 30).

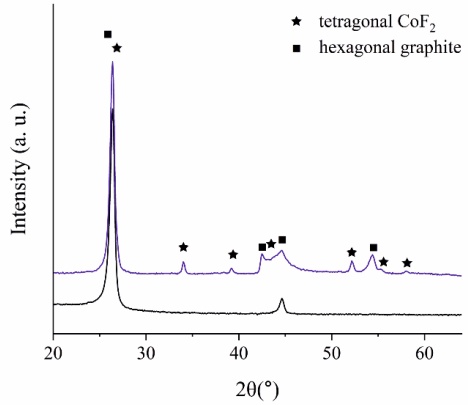

Figure 29 GI-x-ray-diffractograms of a bare graphite substrate and a CoF_2 film deposited on it. Reproduced with permission from article III. Copyright 2023 Authors. Distributed under a Creative Commons Attribution (CC BY 3.0) License.

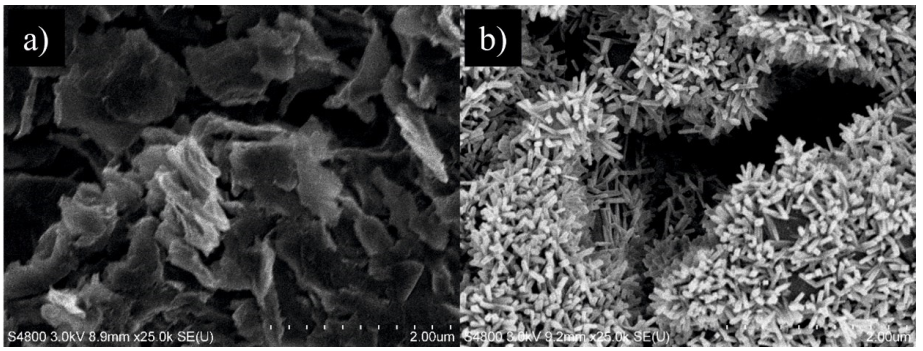

Figure 30 FESEM image of a) a bare graphite substrate and b) a CoF_2 film deposited on graphite at 250 °C. Reproduced with permission from article III. Copyright 2023 Authors. Distributed under a Creative Commons Attribution (CC BY 3.0) License

6.5 NICKEL(II) FLUORIDE

NiF_2 deposition by ALD was studied in article III. Despite the similarities of cobalt(II) fluoride and nickel(II) fluoride, NiF_2 deposition turned out to be more complicated than CoF_2 deposition. NiF_2 deposition was attempted with a process similar to $CoCl_2$TMEDA + NH_4F, i.e. by combining $NiCl_2$(TMPDA) (TMPDA = N,N,N',N',-tetramethyl-1,3-propanediamine)[Ref.128] and NH_4F. No growth was observed, however. Also the well-known precursor combinations of metal thd and TiF_4 or NH_4F were studied, but no film growth was observed. Interestingly, the combinations of $Ni(thd)_2$ and TaF_5 or NbF_5 resulted in film growth, although there are no remarkable differences in the Gibbs free energy

changes for the formation of NiF_2 from $Ni(thd)_2$ and NH_4F, TiF_4, TaF_5, or NbF_5 (Table 5)

Table 5. *Calculated Gibbs free energy changes for the formation of one mole of NiF_2 from $Ni(thd)_2$ and NH_4F, TiF_4, NbF_5, or TaF_5 at 250 °C. NiO has been used as an approximation for the $Ni(thd)_2$*

Fluoride source	ΔG (kJ/mol)
HF (from NH_4F)	-48
TiF_4	-64
NbF_5	-67
TaF_5	-76

The use of NbF_5 as the fluoride source in ALD has been reported in a patent[129], but to our knowledge no research article has been published. Previously NbF_5 has been used as a Nb source in ALD.[115]

The films were grown at 210–250 °C and contained the tetragonal NiF_2 as measured by XRD. However, large hydrogen and oxygen contents were observed in ToF-ERDA measurements. The films were therefore *in-situ* capped with YF_3, but similar H and O contents were detected in the bulk of the NiF_2 films as seen in the ToF-ERDA depth profiles (Fig. 31a). This indicates that the H and O incorporation occurs already during the deposition. Similar H and O contents were observed also when NbF_5 was changed to TaF_5 (Fig. 31b). It is assumed that the hygroscopicity of NiF_2 films is the reason for the H and O incorporation.

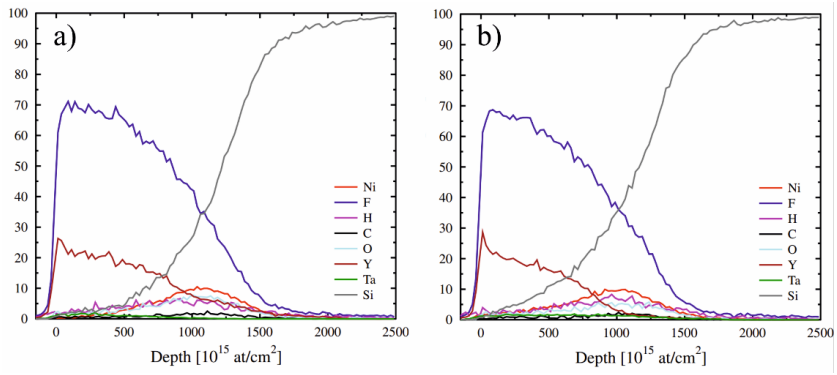

Figure 31 Elemental depth profiles of YF_3-capped NiF_2 films deposited using a) NbF_5 or b) TaF_5 as fluoride source as measured by ToF-ERDA. TaF_5 was used in YF_3 deposition in both cases. Reproduced with permission from article III. Copyright 2023 Authors. Distributed under a Creative Commons Attribution (CC BY 3.0) License.

6.6 HOLMIUM FLUORIDE

One aim of the study on ALD of HoF_3 was to prove further that NbF_5 can be used to grow good-quality metal fluoride films. NbF_5 was combined with $Ho(thd)_3$ to deposit HoF_3.[III] This material has interesting properties for laser applications[130], and no ALD process for HoF_3 has been reported yet.

HoF_3 deposition was studied at temperatures of 200–275 °C. All the films consist of the orthorhombic HoF_3 as measured by XRD (Fig. 32). In FESEM, the films deposited at lower temperatures look quite smooth whereas the films deposited at higher temperatures show distinct flakes (Fig. 33).

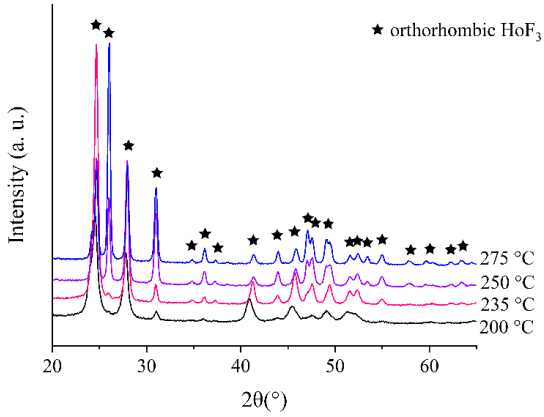

Figure 32 GI-x-ray diffractograms of HoF_3 films deposited at 200–275 °C. Reproduced with permission from article III. Copyright 2023 Authors. Distributed under a Creative Commons Attribution (CC BY 3.0) License.

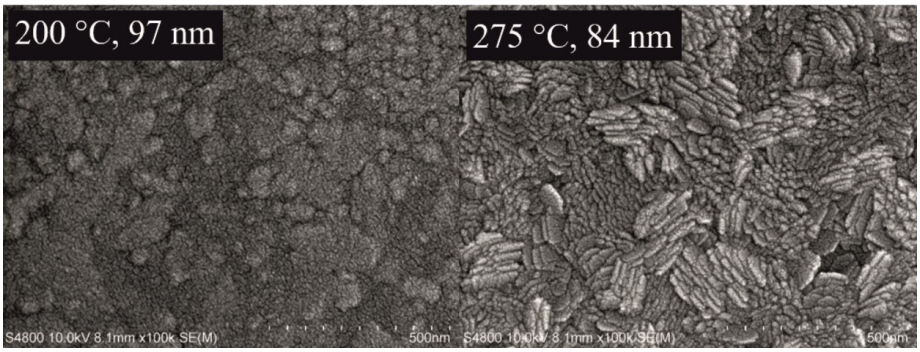

Figure 33 FESEM images of HoF_3 films deposited at 200 °C and 275 °C. Reproduced and adapted with permission from article III. Copyright 2023 Authors. Distributed under a Creative Commons Attribution (CC BY 3.0) License.

Saturation of the growth per cycle with respect to the pulse lengths was achieved at 250 °C as seen in Figure 34. The stoichiometry and elemental contents of the films were measured with ToF-ERDA. The F/Ho ratio varies between 2.9 and 3.4 and is thus in line with XRD. The contents of the light impurities are low in the films deposited at 235 °C and above. The most interesting aspect of this new process is however the low amount of Nb impurities in the films, especially at the deposition temperatures of 250 and 275 °C, where the Nb content is 0.21 and 0.15 at-% (Table 6). The Nb content is lower than the Ti contents in many ALD metal fluoride films deposited with TiF_4 as the fluoride source.

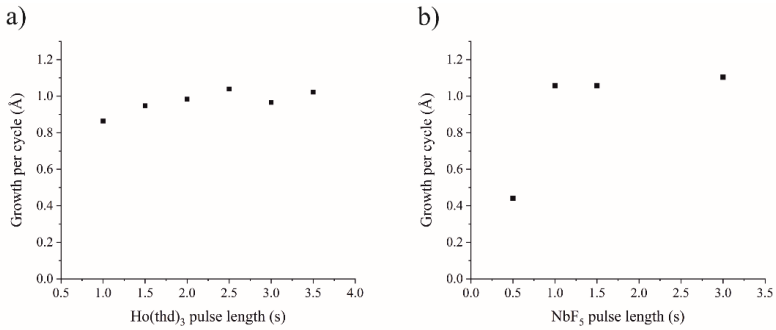

Figure 34 Growth per cycle as a function of a) $Ho(thd)_3$ and b) NbF_5 pulse lengths at a deposition temperature of 250 °C. Reproduced with permission from article III. Copyright 2023 Authors. Distributed under a Creative Commons Attribution (CC BY 3.0) License.

Table 6. *Impurity contents and stoichiometries of HoF_3 films as measured by ToF-ERDA.*

	T_{dep} 200 °C	T_{dep} 235 °C	T_{dep} 250 °C	T_{dep} 275 °C
Ho (at-%)	19.2 ± 0.2	20.5 ± 0.2	23.4 ± 0.2	22.8 ± 0.2
F (at-%)	55.5 ± 1.2	69.9 ± 1.3	73.4 ± 1.5	74.4 ± 1.5
Nb (at-%)	2.3 ± 0.2	1.24 ± 0.12	0.21 ± 0.04	0.15 ± 0.03
H (at-%)	11.2 ± 1.1	4.3 ± 0.6	1.1 ± 0.3	0.7 ± 0.2
C (at-%)	3.7 ± 0.4	1.2 ± 0.2	0.43 ± 0.09	0.30 ± 0.09
N (at-%)	<0.03	<0.07	<0.03	<0.05
O (at-%)	8.1 ± 0.5	2.9 ± 0.2	1.5 ± 0.2	1.6 ± 0.2
F/Ho	2.9	3.4	3.1	3.3

6.7 SCANDIUM FLUORIDE AND SCANDIUM ALUMINIUM FLUORIDE

The motivation for studying scandium fluoride is the thermal expansion properties as described in chapter 2.3. There are not yet ALD processes for materials that have negative thermal expansion coefficients over wide temperature ranges.

An ALD process for ScF_3 was presented in article IV. The ScF_3 process was also combined with an AlF_3 ALD process to make $Sc_xAl_yF_z$ which, with a right cation ratio, has been shown to have a thermal expansion coefficient close to zero.[53]

According to previous tests by our group, the combination of $Sc(thd)_3$ + TiF_4 does not produce any film. NH_4F was therefore chosen as the fluoride precursor and combined with $Sc(thd)_3$. Figure 35 shows the GPC of ScF_3 films as a function of pulse times of $Sc(thd)_3$ and NH_4F at the deposition temperature of 300 °C. The GPC saturates to ~0.2 Å when 1.0 s pulses of $Sc(thd)_3$ are applied. In the case of NH_4F pulses, the GPC shows soft saturation, i.e., the GPC increases softly towards a constant value.

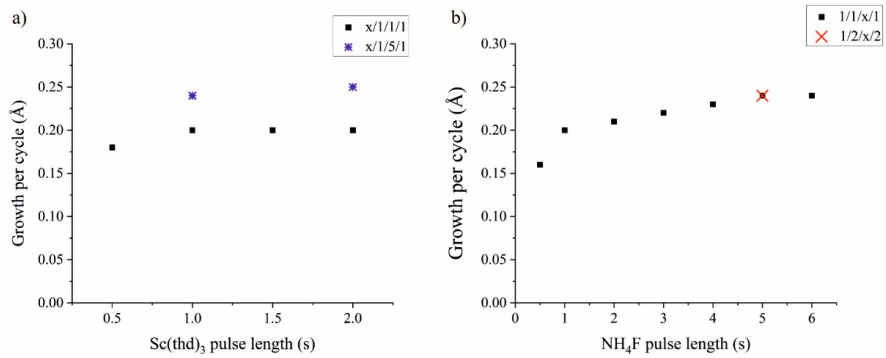

Figure 35 GPC of ScF_3 as a function of a) $Sc(thd)_3$ and b) NH_4F pulse lengths as studied at 300 °C.

The films are crystalline over the whole deposition temperature range (250–375 °C) according to XRD (Fig. 36). The reflections could point to the cubic, hexagonal, or orthorhombic ScF_3, since the diffraction patterns of these phases coincide. The crystal phase was therefore modelled with the MAUD software. The best fit was obtained with the cubic phase, but the fit was not perfect, however. The film was annealed at 300 °C for 4 hours to see if some relaxation of stress would occur. Some relaxation took indeed place, and the fit was improved to some extent.

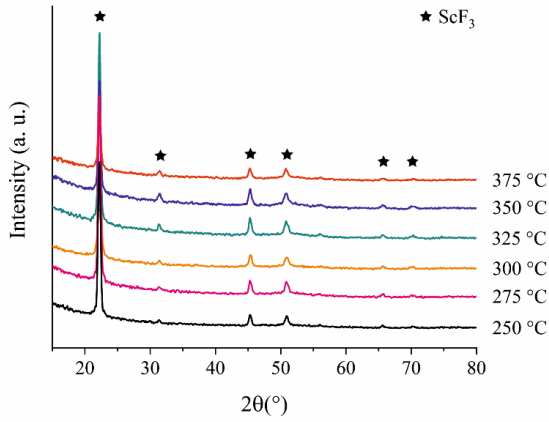

Figure 36 GI-x-ray diffractograms of ScF_3 films deposited at different temperatures.

According to ToF-ERDA, the stoichiometry of the films corresponds well to ScF_3 (Table 7). The impurity contents are in general low, and no nitrogen was detected in the films, which indicates that also in this process the NH_3 formed upon decomposition of NH_4F is not interfering with the film growth.

Table 7. *Stoichiometry and impurity contents of ScF_3 films deposited at 250–350 °C as measured by ToF-ERDA*

	T_{dep} 250 °C	T_{dep} 275 °C	T_{dep} 300 °C	T_{dep} 325 °C	T_{dep} 350 °C
Sc (at-%)	23.6 ± 0.4	24.2 ± 0.5	23.9 ± 0.4	23.7 ± 0.4	23.9 ± 0.5
F (at-%)	72.0 ± 0.9	71.0 ± 1.0	73.5 ± 0.9	72.7 ± 0.8	73.0 ± 0.9
O (at-%)	1.64 ± 0.10	1.33 ± 0.09	1.26 ± 0.08	1.31 ± 0.09	1.22 ± 0.08
N (at-%)	-	-	-	-	-
C (at-%)	0.49 ± 0.06	0.40 ± 0.06	0.23 ± 0.04	0.15 ± 0.02	0.12 ± 0.02
H (at-%)	2.3 ± 0.5	3.0 ± 0.7	1.2 ± 0.3	2.2 ± 0.5	1.8 ± 0.4
F/Sc	3.1	2.9	3.1	3.1	3.1

Thermal expansion of a preheated ScF_3 film was studied by HTXRD in nitrogen atmosphere. Figure 37 shows the intensity of the reflections as a function of the temperature. The 2θ positions of the reflections change only slightly, indicating that no remarkable thermal expansion or contraction occurs. The unit cell parameter a was refined with the MAUD software using the cubic ScF_3 model. Figure 37 shows the unit cell parameter a as a function of the temperature. As seen, the film shrinks upon annealing.

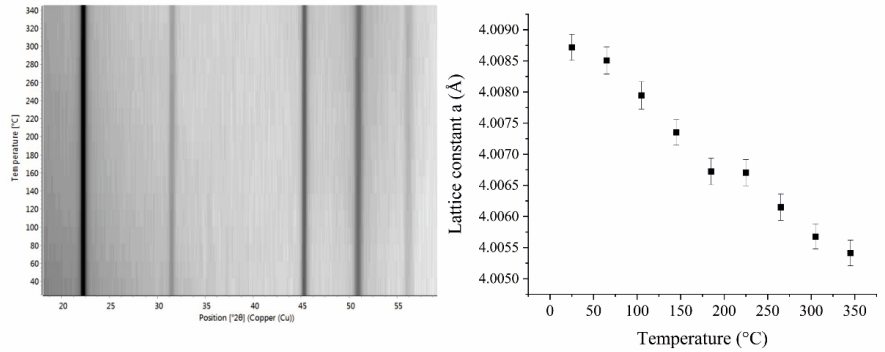

Figure 37 HTXRD of a preheated ScF_3 film and the temperature dependence of the lattice parameter a of the cubic ScF_3 film.

For the $Sc_xAl_yF_z$ deposition, the deposition of AlF_3 was studied first. The deposition was first attempted by using a process analogous to the ScF_3 process to ensure easy combination of the processes. No film growth was obtained with the combination of $Al(thd)_3$ and NH_4F, however. Previously it has been reported that also the combination of $Al(thd)_3$ and TiF_4 does not produce film on Si and poor-quality films were grown on LiF.[Ref. 92] Therefore, the combination of $AlCl_3$ and NH_4F was studied, and film growth was observed. The $Sc_xAl_yF_z$ deposition was done in a supercycle manner by combining the ScF_3 and AlF_3 binary cycles in different ratios. For example, one supercycle consisted of ten $Sc(thd)_3$ + NH_4F binary cycles and one $AlCl_3$ + NH_4F binary cycle.

HTXRD was measured from films with different Sc:Al ratios. In all cases, the positions of the reflections shift to smaller 2θ angles as the temperature is increased, indicating thermal expansion. Figure 38 shows the intensity of the reflections as a function of the temperature for a preheated $Sc_xAl_yF_z$ film with an Al content of 4.3 at-%. The percentual changes in the unit cell parameter as a function of temperature, as compared to room temperature, are shown in Figure 38 for films with different Sc:Al ratios. The larger the Al content is, the more the lattice expands. Thus, the thermal expansion properties of the ScF_3 films can be modified by incorporating Al^{3+} ions into the structure. By further decreasing the Al content, a material with a thermal expansion coefficient close to zero could be obtained.

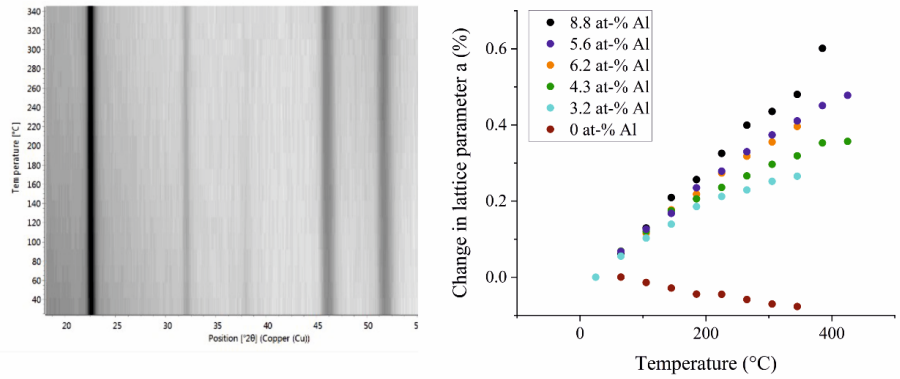

Figure 38 HTXRD of a preheated $Sc_xAl_yF_z$ film and the change (%) in the lattice constant as compared to the lattice constant at room temperature in a ScF_3 film and films with different Sc:Al ratios.

6.8 OTHER METAL FLUORIDES

6.8.1 IRON FLUORIDES

FeF_2 and FeF_3 belong to the most interesting metal fluoride materials for the cathodes in lithium-ion and sodium-ion batteries. In addition, FeF_3 may be combined with ScF_3 to form a close-to-zero thermal expansion material.[47] In this work, ALD deposition of FeF_2 and FeF_3 was attempted with several precursor combinations. In addition, conversion of iron oxides to fluorides was attempted. No well-behaving ALD processes were found, however.

The most interesting results were obtained with the combination of $FeCl_3$ and TiF_4. These experiments resulted at 225–300 °C in $FeCl_2$ films, which formed $FeCl_2$ hydrate upon exposure to air, as measured by XRD (Fig. 39). Interestingly, this result indicates that iron is reduced in the reaction. What would be the reducing agent is not known, however. In SEM (Fig. 39) the films show a morphology typical of 2D materials which $FeCl_2$ indeed is.

The reduction of Fe^{3+} to Fe^{2+} was observed also when $FeCl_3$ and NH_4F were combined. At deposition temperatures higher than 250 °C, the films consisted of FeF_2, whereas at lower temperatures possibly NH_4FeF_4 or FeF_3 was obtained. The FeF_2 films were spotty and blurred rapidly when exposed to air. The spottiness is likely caused by small $FeCl_3$ precursor particles being transported to the substrates. Also the FeF_3 or NH_4FeF_4 films were very nonuniform.

It should be noted that pulsing only $FeCl_3$ on the Si substrate did not produce a $FeCl_2$ film. In addition, Fe_2O_3 can be deposited by the $FeCl_3$ + H_2O ALD process.[131] It is therefore suspected that the fluoride is catalyzing the decomposition of $FeCl_3$ to $FeCl_2$.

Iron fluoride deposition was attempted also indirectly, through iron oxide, by using the pulsing sequence $FeCl_3$ + H_2O + NH_4F. Nonuniform films were obtained. The films probably consist of iron oxide. When the NH_4F pulses were replaced by TiF_4 pulses, films consisting of possibly $Fe_xTi_yO_z$ were obtained. When Fe_2O_3 films were exposed to HF (from NH_4F) for conversion at 300 and 350 °C inside the ALD reactor, the films remained as Fe_2O_3.

All the precursor combinations studied for the FeF_2 and FeF_3 deposition are listed in Table 8. The outcome of each combination is briefly commented.

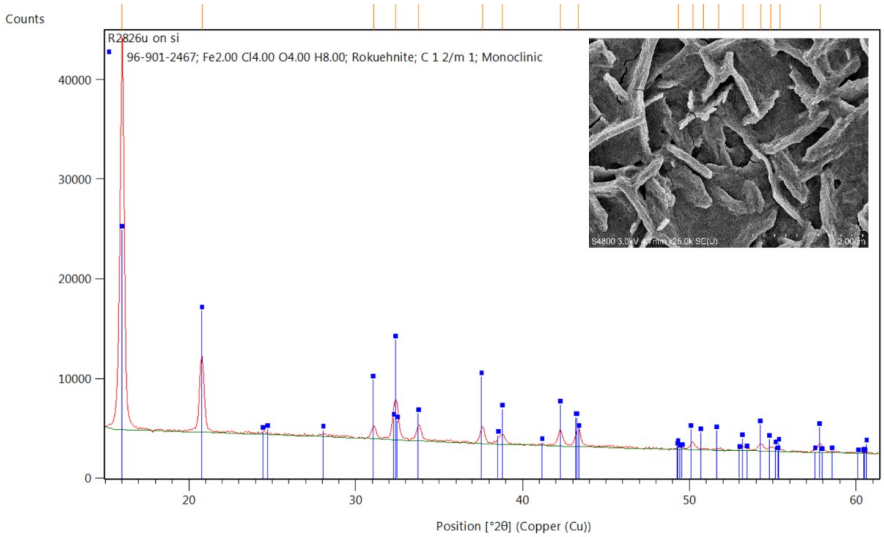

Figure 39 GI-x-ray diffractogram of a $FeCl_2$ x H_2O film obtained with the combination of $FeCl_3$ and TiF_4 and a FESEM image of the same film.

Table 8. *The studied precursor combinations and the results of ALD of FeF_2 and FeF_3*

Precursors	Deposition temperatures	Outcome	Notes
FeF_2			
$FeCp_2 + NH_4F$	150–350 °C	No film	
FeF_3			
$Fe(thd)_3 + NH_4F$	250 °C	No film	
$Fe(thd)_3 + TiF_4$	160–350 °C	No film	Deposition attempted also on AlF_3 and YF_3
$Fe(O^tBu)_3 + NH_4F$	120, 150 °C	No film	
$FeCl_3 + NH_4F$	160–300 °C	$T_{dep} < 250$ °C: FeF_3 or NH_4FeF_4 $T_{dep} > 250$ °C: FeF_2	Spotty, nonuniform films
$FeCl_3 + TiF_4$	200–300 °C	200 °C: no film 225–300 °C: $FeCl_2$ x H_2O	
$FeCl_3 + TaF_5$	180–250 °C	At 250 °C film on YF_3: $FeCl_2$ x H_2O	Deposition attempted also on YF_3
$Fe(acac)_3 + NH_4F$	150–300 °C	Something amorphous growing on the substrates	Deposition attempted also on GdF_3 and Al_2O_3
$Fe(acac)_3 + TiF_4$	150–300 °C	Some growth at 150 °C	Deposition attempted also on ScF_3
Via oxide chemistry			
Pulsing sequence: ($FeCl_3$/purge/H_2O/purge/NH_4F/purge)	200 and 300 °C	Messy films, probably iron oxide	
($FeCl_3$/purge/H_2O/purge/TiF_4/purge/)	200 °C	Probably $Fe_xTi_yO_z$	
Fe_2O_3 films exposed to NH_4F in ALD reactor after deposition	300 and 350 °C	Films remained as iron oxide	

6.8.2 CESIUM FLUORIDE

At the time the deposition of CsF was studied, no ALD process existed for cesium containing compounds. CsF deposition was attempted with the combinations of Csthd and either TiF_4, TaF_5, or NH_4F, and CsHMDS (HMDS=bis(trimethylsilyl)amide) and TiF_4 or NH_4F.

The combination of Csthd and TiF_4 resulted in film growth, but XRD showed the films to consist of many phases, e.g. crystalline $CsTiF_4$, Cs_2SiF_6, and some unidentified phases (Fig. 40). Sometimes cubic CsF was seen together with these other phases. When TiF_4 was changed to TaF_5, crystalline $Cs_7Ta_8O_{13}F_{21}$ and an unidentified phase were obtained. With NH_4F as the fluoride source, a film was obtained, but it could not be identified by XRD. It is possible that part of the XRD reflections originated from Cs_2SiF_6. Also EDS results supported this. It was suspected that HF produced in the decomposition of NH_4F was etching glass parts of the reactor forming volatile SiF_4 or silicon oxyfluoride compounds. SiF_4 or $Si_xO_yF_z$ could eventually end up in the films as Si impurities. These were observed also when sapphire substrates were used, and therefore Si substrates can not to be the only cause for the Si incorporation.

The combination of CsHMDS + NH_4F was studied only at a deposition temperature of 250 °C. It resulted in a strongly crystalline Cs_2SiF_6 phase, which further supports the assumption that Cs_2SiF_6 may have formed in the Csthd + NH_4F/TiF_4 processes. CsHMDS was tested also with TiF_4 at a deposition temperature of 250 °C. Also in this case, the Cs_2SiF_6 phase was observed in XRD, but an unknown additional phase with lower intensity was also detected.

The first ALD-process for a Cs-containing compound, $CsNb_xO_y$, with CsO^tBu, $Nb(OEt)_5$, and H_2O as precursors was published in 2020 by Sønsteby et al.[132] Later, ALD processes for CsI and $CsPbI_3$ were developed by our group.[133] $Cs(N(SiMe_3)_2)$, $Pb(N(SiMe_3)_2)_2$, and SnI_4 were used as precursors.

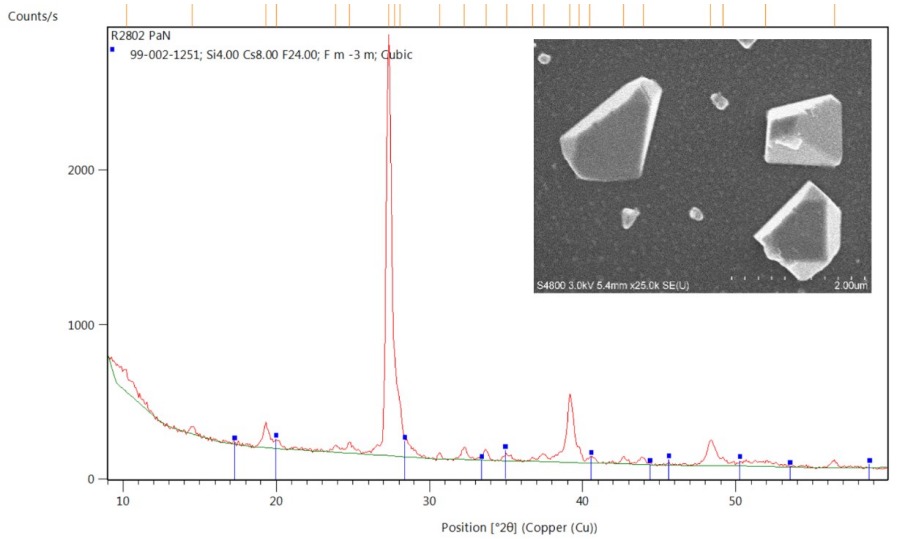

Figure 40 GI-x-ray diffractogram of a film deposited with Csthd and TiF_4 shows the possible Cs_2SiF_6 phase and an unidentified phase. FESEM image of the same film shows the unidentified crystals.

7 CONCLUSIONS AND OUTLOOK

Atomic layer deposition (ALD) is one of the most sophisticated thin film deposition methods, known especially from its significant role in the semiconductor industry. Accordingly, much research efforts have been put into the research of ALD of e.g. metal oxides, sulfides, nitrides and metals. Many metal fluorides, in turn, still lack an ALD process, although new important applications also exist. This work was aimed to increase the number and knowledge of ALD processes for metal fluorides. Although the topic was chosen based on the basic research viewpoint, the materials studied were selected so that several applications were addressed. The work presents new ALD processes for TbF_3, GdF_3, CoF_2, NiF_2, HoF_3, ScF_3, and $Sc_xAl_yF_z$.

Either TiF_4, NH_4F, or NbF_5 was used as the fluoride source in the new ALD processes. In general, the rare earth metal fluoride processes produced pure and crystalline films, no matter which fluoride source was used. As an example, it was possible to deposit TbF_3 by using TiF_4 without Ti impurity incorporation, in contrast to the earlier reports on ALD of rare earth metal fluorides deposited with TiF_4 as the fluoride source. An ALD process using NbF_5 as the fluoride source was reported for the first time. HoF_3 deposition by using $Ho(thd)_3$ and NbF_5 as the precursors served as the model example. NbF_5 turned out to be a potential fluoride source: the Nb content in the films was low. NbF_5 also produced films in a case when TiF_4 and NH_4F did not. In addition to the binary metal fluorides, ternary metal fluorides were studied. GdF_3 films were converted to $NaGdF_4$ by exposing them to Nathd vapor. The ScF_3 process was in turn combined with an AlF_3 ALD process to make $Sc_xAl_yF_z$ films.

Transition metal fluorides are a more heterogeneous group than the rare earth fluorides. The CoF_2 process was successful depositing pure films, whereas the NiF_2 film deposition was troublesome due to the hygroscopicity of NiF_2. For FeF_x, no well-working ALD process was found despite many studied precursor combinations.

The studied rare earth fluorides may have applications as antireflection coatings, in thermal expansion tuning, and in luminescence applications, such as in bioimaging. The transition metal fluorides were mainly studied for lithium-ion and sodium-ion battery electrodes. Importantly, in the abovementioned applications the versatility of the ALD method is demonstrated in an excellent way. The ability of ALD to deposit uniform films with precise thickness is essential for antireflection coatings, whereas conformal coatings on nanoparticles are needed for bioimaging and uniformly distributed dopants for luminescent devices in general.

Still many binary metal fluorides lack an ALD process. Based on the similar nature of the rare earth elements, it can be expected that ALD chemistry can be found also for the remaining rare earth fluorides. For the transition metal

fluorides, the case is more complicated. However, chemistry analogous to the $CoCl_2$TMEDA + NH_4F would be interesting to test at least for FeF_2 deposition, since the combination of $FeCl_3$ and NH_4F resulted in FeF_2 films.

The number of ternary metal fluorides deposited by ALD is still very small. The binary metal fluoride processes developed in this work serve however as the basis for many interesting ternary metal fluorides, such as the already mentioned $NaGdF_4$. Ternary metal fluorides include also the interesting material group of transition metal oxyfluorides. These materials have been investigated as cathode materials for LIB's. Compared to transition metal fluorides, transition metal oxyfluorides have better electronic conductivities and thus could overcome the main issue related to the transition metal fluoride cathodes.

REFERENCES

1. Leskelä, M. & Ritala, M. Atomic Layer Deposition Chemistry: Recent Developments and Future Challenges. Angew. Chem. Int. Edit. **42**, 5548–5554 (2003).
2. Zardetto, V., Williams, B. L., Perrotta, A., Di Giacomo, F., Verheijen, M. A., Andriessen, R., Kessels, W. M. M. & Creatore, M. Atomic Layer Deposition for Perovskite Solar Cells: Research Status, Opportunities and Challenges. Sustainable Energy Fuels **1**, 30–55 (2017).
3. Leskelä, M., Salmi, E. & Ritala, M. Atomic Layer Deposited Protective Layers. Mater. Sci. Forum **879**, 1086–1092 (2017).
4. Jarmo Maula, J. M. Atomic Layer Deposition for Industrial Optical Coatings. Chin. Opt. Lett. **8**, 53–58 (2010).
5. Ritala, M. & Niinistö, J. Industrial Applications of Atomic Layer Deposition. ECS Trans. **25**, 641–652 (2009).
6. Miikkulainen, V., Leskelä, M., Ritala, M., Puurunen, R. L. & Leskelä, M. Crystallinity of Inorganic Films Grown by Atomic Layer Deposition: Overview and General Trends J. Appl. Phys. **113**, 123521 (2013).
7. Hennessy, J., Jewell, A. & Nikzad, S. (Invited) ALD Metal Fluorides for Ultraviolet Filter and Reflective Coating Applications. ECS Trans. **80**, 107–118 (2017).
8. Mäntymäki, M., Ritala, M. & Leskelä, M. Metal Fluorides as Lithium-Ion Battery Materials: An Atomic Layer Deposition Perspective. Coatings, **8**, 277 (2018).
9. Lemoine, K., Hémon-Ribaud, A., Leblanc, M., Lhoste, J., Tarascon, J-M. & Maisonneuve, V. Fluorinated Materials as Positive Electrodes for Li- and Na-Ion Batteries. Chem. Rev. **122**, 14405–14439 (2022).
10. Li, C., Xu, L., Liu, Z., Li, Z., Quan, Z., Al Kheraifd, A. A. & Lin, J. Current Progress in the Controlled Synthesis and Biomedical Applications of Ultrasmall Nanoparticles. Dalton Trans. **47**, 8538–8556 (2018).
11. Keshavarz Hedayati, M. & Elbahri, M. Antireflective Coatings: Conventional Stacking Layers and Ultrathin Plasmonic Metasurfaces, A Mini-Review. Materials, **9**, 497 (2016)
12. Yoldas, B. E. Investigations of Porous Oxides as an Antireflective Coating for Glass Surfaces. Appl. Optics, **19**, 1425–1429 (1980).
13. Buskens, P., Burghoorn, M., Mourad, M. C. D. & Vroon, Z. Antireflective Coatings for Glass and Transparent Polymers. Langmuir **32**, 6781–6793 (2016).
14. Yoshida, T., Nishimoto, K., Sekine, K. & Etoh, K. Fluoride Antireflection Coatings for Deep Ultraviolet Optics Deposited by Ion-Beam Sputtering. Appl. Optics, **45**, 1375–1379 (2006).
15. Khan, L. U. & Khan, Z. U. Rare earth luminescence: Electronic Spectroscopy and Applications. in Handbook of Materials Characterization (eds. Sharma, S.) 345–404 (Springer, 2018).
16. Lucas, J., Lucas, P., Le Mercier, T., Rollat, A. & Davenport, W. Introduction to Rare Earth Luminescent Materials. in Rare Earths - Science, Technology, Production and use, 251–280 (Elsevier, 2015)

17. Naccache, R., Yu, Q. & Capobianco, J. A. The Fluoride Host: Nucleation, Growth, and Upconversion of Lanthanide-Doped Nanoparticles. Adv. Opt. Mater. **3**, 482–509 (2015).
18. Wegh, R. T., Donker, H., Oskam, K. D. & Meijerink, A. Visible Quantum Cutting in $LiGdF_4:Eu^{3+}$ Through Downconversion. Science, **283**, 663–666 (1999).
19. DaCosta, M. V., Doughan, S., Han, Y. & Krull, U. J. Lanthanide Upconversion Nanoparticles and Applications in Bioassays And Bioimaging: A review. Anal. Chim. Acta **832**, 1–33 (2014).
20. Kahng, D. Electroluminescence of Rare-Earth and Transition Metal Molecules in II-VI Compounds via Impact Excitation. Appl. Phys. Lett. **13**, 210–212 (1968).
21. Huang, X., Han, S., Huang, W. & Liu, X. Enhancing Solar Cell Efficiency: The Search for Luminescent Materials as Spectral Converters. Chem. Soc. Rev. **42**, 173–201 (2012).
22. Cheng, R., Chen, Y., Li, Z., Chen, X., Yang, P., Zhu, H., Huang, Y., Sun, Z. & Huang, S. Citric Acid-Assisted Growth of Lanthanide Ions Co-Doped One-Dimensional Upconversion Microcrystals and Their Photovoltaic Applications. J. Mater. Sci.-Mater. El. **25**, 4066–4073 (2014).
23. Shen, J., Li, Z., Cheng, R., Luo, Q., Luo Y., Chen, Y., Chen, X., Sun, Z. & Huang, S. Eu^{3+}-doped $NaGdF_4$ Nanocrystal Down-converting Layer for Efficient Dye-sensitized Solar Cells. ACS Appl. Mater. Inter. **6**, 17454–17462 (2014).
24. Allen, T. G., Bullock, J., Yang, X., Javey, A. & De Wolf, S. Passivating Contacts for Crystalline Silicon Solar Cells. Nature Energy **4**, 914–928 (2019).
25. Chen, Z., Lin, W., Liu, Z., Cai, L., Chen, Y., Ai, B., Liang, Z., Gao, P. & Shen, H. Yttrium Fluoride-Based Electron-Selective Contacts for Crystalline Silicon Solar Cells. ACS Appl. Energy Mater. **4**, 2158–2164 (2021).
26. Wang, W., Cai, l., Meng, L., Zhang, l., Chen, N., Shen, H. & Liang, Z. Cerous Fluoride Dopant-Free Electron-Selective Contact for Crystalline Silicon Solar Cells. Phys. Status Solidi-R. **15**, 2100135 (2021).
27. Zhang, L., Meng, L., Cai, L., Chen, Z., Lin, W., Chen, N., Wang, W., Shen, H & Liang, H. High-Performance Europium Fluoride Electron-Selective Contacts for Efficient Crystalline Silicon Solar Cells. Solar RRL **5**, 2100057 (2021).
28. Chen, N., Cai, L., Xie, F., Wang, W., Wei, H., Hong, Y., Shen, H. & Liang, Z. Gadolinium Fluoride as a High-Thickness-Tolerant Electron-Selective Contact Material for Solar Cells. ACS Appl. Energy Mater. **5**, 4351–4357 (2022).
29. Yu, X., Zhang, H. & Yu, J. Luminescence Anti-counterfeiting: From Elementary to Advanced. Aggregate **2**, 20–34 (2021).
30. Hu, Y., Shao, Q., Deng, X., Song, D., Han, S., Dong, Y. & Jianqing, J. Thermally Induced Multicolor Emissions of Upconversion Hybrids with Large Color Shifts for Anticounterfeiting Applications. J. Mater. Chem. C **7**, 11770–11775 (2019).
31. Zhao, Q., Zhao, J., Tao, M., Wang, C., Zeng, X., Hu, Y., Wang, S., Zeng, M., Zhou, W., Gu, H., Li, Y. Controllable Planar Electrodeposition of $NaYF_4$: Yb^{3+}, Er^{3+} Thin Films with Efficient Upconverting Fluorescence. J. Lumin. **214**, 116580 (2019).
32. Dong, Y., Zhao, H., Wang, S., Cheng, Q., Liu, S. & Li, Y. Multimode Anticounterfeiting Labels Based on a Flexible and Water-Resistant

$NaGdF_4$:Yb^{3+},Er^{3+}@Carbon Dots Chiral Fluorescent Cellulose Film. ACS Appl. Mater. Inter. **14**, 40313–40321 (2022).

33. Ye, S., Xiao, F., Pan, Y. X., Ma, Y. Y. & Zhang, Q. Y. Phosphors in Phosphor-Converted White Light-Emitting Diodes: Recent Advances in Materials, Techniques and Properties. Mat. Sci. Eng. R. **71**, 1–34 (2010).
34. Fang, M. H., Bao, Z., Huang, W. T. & Liu, R. S. Evolutionary Generation of Phosphor Materials and Their Progress in Future Applications for Light-Emitting Diodes. Chem. Rev. **122**, 11474–11513 (2022).
35. Sayed, F. N., Grover, V., Dubey, K. A., Sudarsan, V. & Tyagi, A. K. Solid State White Light Emitting Systems Based on CeF_3:RE^{3+} Nanoparticles and Their Composites with Polymers. J. Colloid Interface Sci. **353**, 445–453 (2011).
36. Li, D., Ma, Q., Song, Y., Xi, X., Dong, X., Yu, W., Wang, J. & Liu, G., Tunable Multicolor Luminescence and White Light Emission Realized in Eu^{3+} Mono-Activated GdF_3 Nanofibers with Paramagnetic Performance. RSC Adv. **6**, 113045–113052 (2016).
37. Sharma, R. K., Mudring, A. V. & Ghosh, P. Recent Trends in Binary and Ternary Rare-Earth Fluoride Nanophosphors: How Structural and Physical Properties Influence Optical Behavior. J. Lumin. **189**, 44–63 (2017).
38. Song, C., Zhang, S., Zhou, Q., Hai, H., Zhao, D. & Hui, Y. Upconversion Nanoparticles for Bioimaging. Nanotechnol. Rev. **6**, 233–242 (2017).
39. Vetrone, F., Naccache, R., Mahalingam, V., Morgan, C. G. & Capobianco, J. A. The Active-Core/Active-Shell Approach: A Strategy to Enhance the Upconversion Luminescence in Lanthanide-Doped Nanoparticles. Adv. Funct. Mater. **19**, 2924–2929 (2009).
40. Rashid, H. U., Utrera Martines M. A., Jorge J., Martin de Moraes, P., Umar, M. N., Khan K. & Rehman, H.U. Cyclen-based Gd^{3+} Complexes as MRI Contrast Agents: Relaxivity Enhancement and Ligand design. Bioorgan. Med. Chem. **24**, 5663–5684 (2016).
41. Geraldes, C. F. G. C. & Laurent, S. Classification and Basic Properties of Contrast Agents for Magnetic Resonance Imaging. Contrast Media Mol. I. **4**, 1–23 (2009).
42. Xiong, L. Q., Chen, Z. G., Yu, M. X., Li, F. Y., Liu. C. & Huang, C. H. Synthesis, Characterization, and In Vivo Targeted Imaging of Amine-Functionalized Rare-Earth Up-Converting Nanophosphors. Biomaterials **30**, 5592–5600 (2009).
43. Greve, B. K., Martin, K. L., Lee, P. L., Chupas, P. J., Chapman, K. W. & Wilkinson, A. P. Pronounced Negative Thermal Expansion from a Simple Structure: Cubic ScF_3. J. Am. Chem. Soc. **132**, 15496–15498 (2010).
44. Bocharov, D., Krack, M., Kalinko, A., Purans, J., Rocca, F., Ali, S. E. & Kuzmin, A. Ab Initio Molecular Dynamics Simulations of the Sc K-edge EXAFS of Scandium Trifluoride. J. Phys. Conf. Ser. **712**, 012009 (2016).
45. Dove, M. T., Du, J., Wei, Z., Keen, D. A., Tucker, M. G. & Phillips, A. E Quantitative Understanding of Negative Thermal Expansion in Scandium Trifluoride from Neutron Total Scattering Measurements. Phys. Rev. B **102**, 94105 (2020).
46. Handunkanda, S. U., Occhialini, C. A., Said, A. H. & Hancock, J. N. Two-dimensional Nanoscale Correlations in the Strong Negative Thermal Expansion Material ScF_3. Phys. Rev. B **94**, 214102 (2016).
47. Qin, F., Chen, J., Aydemir, U., Sanson, A., Wang, L., Pan, Z., Xu, J., Sun, C., Ren, Y., Deng, J., Yu, R., Hu, L., Jeffrey Snyder, G. & Xing, X. Isotropic

Zero Thermal Expansion and Local Vibrational Dynamics in $(Sc,Fe)F_3$. Inorg. Chem. **56**, 10840–10843 (2017).

48. Kasatkin, I. A., Gulina, L. B., Platonova, N. V., Tolstoy, V. P. & Murin, I. V. Strong Negative Thermal Expansion in the Hexagonal Polymorph of ScF_3. Cryst. Eng. Comm. **20**, 2768–2771 (2018).
49. Evans, J. S. O. Negative Thermal Expansion Materials. J. Chem. Soc., Dalton Trans. **19**, 3317–3326 (1999)
50. Tietz, F. Thermal Expansion of SOFC Materials. Ionics **5**, 129–139 (1999).
51. Morelock, C. R., Greve, B. K., Gallington, L. C., Chapman, K. W. & Wilkinson, A. P. Negative Thermal Expansion and Compressibility of $Sc_{1-x}Y_xF_3$ ($x \leq 0.25$). J. Appl. Phys. **114**, 213501 (2013).
52. Morelock, C. R., Gallington, L. C. & Wilkinson, A. P. Evolution of Negative Thermal Expansion and Phase Transitions in $Sc_{1-x}Ti_xF_3$. Chem.Mater. **26**, 1936–1940 (2014).
53. Morelock, C. R., Gallington, L. C. & Wilkinson, A. P. Solid Solubility, Phase Transitions, Thermal Expansion, and Compressibility in $Sc_{1-x}Al_xF_3$. J. Solid State Chem. **222**, 96–102 (2015).
54. Wang, T., Xu, J., Hu, L., Wang, W., Huang, R., Han, F., Pan, Z., Deng, J., Ren, Y., Li, L., Chen, J. & Xing, X. Tunable Thermal Expansion and Magnetism in Zr-doped ScF_3. Appl. Phys. Lett. **109**, 181901 (2016).
55. Hu, L., Chen, J., Fan, L., Ren, Y., Rong, Y., Pan, Z., Deng, J., Yu, R. & Xing, X. Zero Thermal Expansion and Ferromagnetism in Cubic $Sc_{1-x}M_xF_3$ (M = Ga, Fe) Over a Wide Temperature Range. J. Am. Chem. Soc. **136**, 13566–13569 (2014).
56. Xiao, N., Qiao, Y. Q., Shi, N. K., Song, Y. Z., Deng, S. Q. & Chen, J., Realization of high thermal conductivity and tunable thermal expansion in the ScF_3@Cu core-shell composites. Sci. China Technol. Sci. **64**, 2057–2065 (2021).
57. Liu, W., Placke, T. & Chau, K. T. Overview of Batteries and Battery Management for Electric Vehicles. Energy Reports **8**, 4058–4084 (2022).
58. Zhang, W., Lu, J. & Guo, Z. Challenges and Future Perspectives on Sodium and Potassium Ion Batteries for Grid-Scale Energy Storage. Materials Today **50**, 400–417 (2021).
59. Liu, C., Neale, Z. G. & Cao, G. Understanding Electrochemical Potentials of Cathode Materials in Rechargeable Batteries. Materials Today **19**, 109–123 (2016).
60. Wang, F., Rober, R., Chernova, N. A., Pereira, N., Omenya, F., Badway, F., Hua, X., Ruotolo, M., Zhang, R., Wu, L., Volkov, V., Su, D., Key, B., Whittingham, M. S., Grey, C. P., Amatucci, G. G., Zhu, Y. & Graetz, J. Conversion Reaction Mechanisms in Lithium Ion Batteries: Study of the Binary Metal Fluoride Electrodes. J. Am. Chem. Soc. **133**, 18828–18836 (2011).
61. Deng, D. Li-ion Batteries: Basics, Progress, and Challenges. Energy Sci. Eng. **3**, 385–418 (2015).
62. Wang, L., Wu, Z., Zou, J., Gao, P., Niu, X., Li, H. & Chen, L. Li-free Cathode Materials for High Energy Density Lithium Batteries. Joule **3**, 2086–2102 (2019).
63. Amatucci, G. G. & Pereira, N. Fluoride Based Electrode Materials for Advanced Energy Storage Devices. J. Fluor. Chem. **128**, 243–262 (2007).
64. Arai, H., Okada, S., Sakurai, Y. & Yamaki, J. I. Cathode Performance and Voltage Estimation of Metal Trihalides. J. Power Sources **68**, 716–719 (1997).

65. Badway, F., Pereira, N., Cosandey, F. & Amatucci, G. G. Carbon-Metal Fluoride Nanocomposites: Structure and Electrochemistry of FeF_3:C. J. Electrochem. Soc. **150**, A1209 (2003).
66. Badway, F., Cosandey, F., Pereira, N. & Amatucci, G. G. Carbon Metal Fluoride Nanocomposites: High-Capacity Reversible Metal Fluoride Conversion Materials as Rechargeable Positive Electrodes for Li Batteries. J. Electrochem. Soc. **150**, A1318 (2003).
67. Fu, Z.W., Li, C. L., Liu, W. Y., Ma, J., Wang, Y. & Qin, Q. Z. Electrochemical Reaction of Lithium with Cobalt Fluoride Thin Film Electrode. J. Electrochem. Soc. **152**, E50 (2005).
68. Groult, H., Neveu, S., Leclerc, S., Porras-Gutierrez, A.-G, Julien, C.M., Tressaud, A., Durand, E., Penin, N. & Labrugere, C. Nano-CoF_3 Prepared by Direct Fluorination with F_2 Gas: Application as Electrode Material in Li-ion Battery. J. Fluor. Chem. **196**, 117–127 (2017).
69. Fu, W., Zhao, E., Sun, Z., Ren, X., Magasinski, A. & Yushin, G. Iron Fluoride–Carbon Nanocomposite Nanofibers as Free-Standing Cathodes for High-Energy Lithium Batteries. Adv. Funct. Mater. **28**, 1801711 (2018).
70. Suntola, T. & Antson, J. US4058430A (1977).
71. Kol'tsov, S. I. & Aleskovskii, V. B. Zh. Prikl. Khim. **40**, 907 (1967).
72. Puurunen, R. L. A Short History of Atomic Layer Deposition: Tuomo Suntola's Atomic Layer Epitaxy. Chem. Vapor Depos. **20**, 332–344 (2014).
73. Rönn, J., Karvonen, L., Kauppinen, C., Pyymaki Perros, A., Peyghambarian, N., Lipsanen, H., Säynätjoki, A. & Sun, Z. Atomic Layer Engineering of Er-Ion Distribution in Highly Doped Er:Al_2O_3 for Photoluminescence Enhancement. ACS Photonics **3**, 2040–2048 (2016).
74. Ritala, M. & Niinistö, J. Atomic Layer Deposition. in Chemical Vapour Deposition: Precursors, Processes and Applications (eds. Jones, A. C. & Hitchman, M. L.) 158-206 (Royal Society of Chemistry, 2008)
75. Pessa, M., Huttunen, P. & Herman, M. A. Atomic Layer Epitaxy and Characterization of CdTe Films Grown on CdTe (110) Substrates. J. Appl. Phys. **54**, 6047–6050 (1983).
76. Hartmann, J. M., Cibert, J., Kany, F., Mariette, H., Charleux, M., Alleysson, P., Langer, R. & Feuillet, G. CdTe/MgTe Heterostructures: Growth by Atomic Layer Epitaxy and Determination of MgTe Parameters. J. Appl. Phys. **80**, 6257–6265 (1996).
77. Herman, M. A., Jylhä, O. & Pessa, M. Atomic Layer Epitaxy of $Cd_{1-x}Mn_xTe$ Grown on CdTe (111)B Substrates. J. Cryst. Growth **66**, 480–483 (1984).
78. Yao, T. & Takeda, T. Growth Process in Atomic Layer Epitaxy of Zn Chalcogenide Single Crystalline Films on (100)GaAs. Appl. Phys. Lett. **48**, 160–162 (1986).
79. Ahonen, M., Pessa, M. & Suntola, T. A Study of ZnTe Films Grown on Glass Substrates Using an Atomic Layer Evaporation Method. Thin Solid Films **65**, 301–307 (1980).
80. Aaltonen, T., Alén, P., Ritala, M. & Leskelä, M. Ruthenium Thin Films Grown by Atomic Layer Deposition. Chem. Vapor Depos. **9**, 45–49 (2003).
81. Niinistö, L., Päiväsaari, J., Niinistö, J., Putkonen, M. & Nieminen, M. Advanced Electronic and Optoelectronic Materials by Atomic Layer Deposition: An Overview with Special Emphasis on Recent Progress in Processing of High-K Dielectrics and Other Oxide Materials. Phys. Stat. Sol. (a) **201**, 1443–1452 (2004).
82. Hennessy, J. & Nikzad, S. Atomic Layer Deposition of Lithium Fluoride Optical Coatings for the Ultraviolet. Inorganics **6**, 46 (2018).

83. Hennessy, J., Jewell, A. D., Greer, F., Lee, M. C. & Nikzad, S. Atomic Layer Deposition of Magnesium Fluoride via Bis(ethylcyclopentadienyl)magnesium and Anhydrous Hydrogen Fluoride. J. Vac. Sci. Technol. A **33**, 01A125 (2015).
84. Jones, J.-P., Hennessy, J., Billings, K. J., Krause, F. C., Pasalic, J. & Bugga, R. V. Communication—Atomic Layer Deposition of Aluminum Fluoride for Lithium Metal Anodes. J. Electrochem. Soc. **167**, 060502 (2020).
85. Lee, Y., Sun, H., Young, M. J. & George, S. M. Atomic Layer Deposition of Metal Fluorides Using HF-Pyridine as the Fluorine Precursor. Chem. Mater. **28**, 2022–2032 (2016).
86. Ylilammi, M. & Ranta-aho, T. Metal Fluoride Thin Films Prepared by Atomic Layer Deposition. J. Electrochem. Soc. **141**, 1278–1284 (1994).
87. Pilvi, T., Hatanpää, T., Puukilainen, E., Arstila, K., Bischoff, M., Kaiser, U., Kaiser, N., Leskelä, M. & Ritala, M. Study of a Novel ALD Process for Depositing MgF_2 Thin Films. J. Mater. Chem. **17**, 5077–5083 (2007).
88. Pilvi, T., Arstila, K., Leskelä, M. & Ritala, M. Novel ALD Process for Depositing CaF_2 Thin Films. Chem. Mater. **19**, 3387–3392 (2007).
89. Pilvi, T., Puukilainen, E., Munnik, F., Leskelä, M. & Ritala, M. ALD of YF_3 Thin Films from TiF_4 and $Y(thd)_3$ Precursors. Chem. Vapor Depos. **15**, 27–32 (2009).
90. Pilvi, T., Puukilainen, E., Arstila, K., Leskelä, M. & Ritala, M. Atomic Layer Deposition of LaF_3 Thin Films using $La(thd)_3$ and TiF_4 as Precursors. Chem. Vapor Depos. **14**, 85–91 (2008).
91. Pilvi, T., Puukilainen, E., Kreissig, U., Leskelä, M. & Ritala, M. Atomic Layer Deposition of MgF_2 Thin Films Using TaF_5 as a Novel Fluorine Source. Chem. Mater. **20**, 5023–5028 (2008).
92. Mäntymäki, M., Heikkilä, M. J., Puukilainen, E., Mizohata, K., Marchand, B., Räisänen, J., Ritala, M. & Leskelä, M. Atomic Layer Deposition of AlF_3 Thin Films Using Halide Precursors. Chem. Mater. **27**, 604–611 (2015).
93. Nieminen, H.-E. & Ritala, M. Reaction Mechanism Studies on Atomic Layer Deposition Process of AlF_3. J. Vac. Sci. Technol. A **40**, 022401 (2022).
94. Park, J. S., Mane, A. U., Elam, J. W. & Croy, J. R. Amorphous Metal Fluoride Passivation Coatings Prepared by Atomic Layer Deposition on $LiCoO_2$ for Li-ion Batteries. Chem. Mater. **27**, 1917–1920 (2015).
95. Putkonen, M., Szeghalmi, A., Pippel, E. & Knez, M. Atomic Layer Deposition of Metal Fluorides Through Oxide Chemistry. J. Mater. Chem. **21**, 14461–14465 (2011).
96. Hornsveld, N., Kessels, W. M. M., Synowicki, R. A. & Creatore, M. Atomic Layer Deposition of LiF Using $LiN(SiMe_3)_2$ and SF_6 Plasma. Phys. Chem. Chem. Phys. **23**, 9304–9314 (2021).
97. Vos, M. F. J., Knoops, H. C. M., Synowicki, R. A., Kessels, W. M. M. & Mackus, A. J. M. Atomic Layer Deposition of Aluminum Fluoride Using $Al(CH_3)_3$ and SF_6 Plasma. Appl. Phys. Lett. **111**, 113105 (2017).
98. Fan, K. M., Lai, C. S., Peng, H. K., Lin, S. J. & Lee, C. Y. Improvements on Interface Reliability and Capacitance Dispersion of Fluorinated ALD-Al_2O_3 Gate Dielectrics by CF_4 Plasma Treatment. J. Electrochem. Soc. **155**, G51 (2008).
99. Mäntymäki, M., Mizohata, K., Heikkilä, M. J., Räisänen, J., Ritala, M. & Leskelä, M. Studies on Li_3AlF_6 Thin Film Deposition Utilizing Conversion Reactions of Thin Films. Thin Solid Films **636**, 26–33 (2017).

100.Xie, J., Sendek, A. D., Cubuk, E. D., Zhang, X., Lu, Z., Gong, Y., Wu, T., Shi, F. Liu, W., Reed, E. J., & Cui, Y. Atomic Layer Deposition of Stable $LiAlF_4$ Lithium Ion Conductive Interfacial Layer for Stable Cathode Cycling. ACS Nano **11**, 7019–7027 (2017).

101.Mahuli, N., Cavanagh, A. S. & George, S. M. Atomic Layer Deposition of Aluminum Oxyfluoride Thin Films with Tunable Stoichiometry. J. Vac. Sci. Technol. A **38**, 022407 (2020).

102.Choi, Y. J. & Park, H. H. A Simple Approach to the Fabrication of Fluorine-Doped Zinc Oxide Thin Films by Atomic Layer Deposition at Low Temperatures and an Investigation into the Growth Mode. J. Mater. Chem. C **2**, 98–108 (2013).

103. Mahuli, N., Cavanagh, A. & George, S. M. Atomic Layer Deposition of Hafnium and Zirconium Oxyfluoride Thin Films. J. Vac. Sci. Technol. A **39**, 022403 (2021).

104.Mäntymäki, M., Hämäläinen, J., Puukilainen, E., Munnik, F., Ritala, M. & Leskelä, M. Atomic Layer Deposition of LiF Thin Films from Lithd and TiF_4 Precursors. Chem. Vapor Depos. **19**, 111–116 (2013).

105.Tiurin, O., Solomatin, N., Auinat, M. & Ein-Eli, Y. Atomic Layer Deposition (ALD) of Lithium Fluoride (LiF) Protective Film on Li-ion Battery $LiMn_{1.5}Ni_{0.5}O_4$ Cathode Powder Material. J. Power Sources **448**, 227373 (2020).

106.Chen, L., Chen, K.-S., Chen, X., Ramirez, G., Huang, Z., Geise, N. R., Steinrück, H.-G., Fisher, B- L., Shahbazian-Yassar, R., Toney, M. F., Hersam, M. C. & Elam, J. W. Novel ALD Chemistry Enabled Low-Temperature Synthesis of Lithium Fluoride Coatings for Durable Lithium Anodes. ACS Appl. Mater. Inter. **10**, 26972–26981 (2018).

107.Kvalvik, J. N., Kvamme, K. B., Almaas, K., Ruud, A., Sønsteby, H. H., Nilsen, O. LiF by Atomic Layer Deposition—Made Easy. J. Vac. Sci. Technol. A **38**, 050401 (2020).

108.Lee, Y., Piper, D. M., Cavanagh, A. S., Young , M. J., Lee, S. H. & George, S. M. Atomic Layer Deposition of LiF and Lithium Ion Conducting $(AlF_3)(LiF)_x$ Alloys Using Trimethylaluminum, Lithium Hexamethyldisilazide and Hydrogen Fluoride. ChemRxiv (2017).

109.Mäntymäki, M., Hämäläinen, J., Puukilainen, E., Sajavaara, T., Ritala, M. & Leskelä, M. Atomic Layer Deposition of LiF Thin Films from Lithd, $Mg(thd)_2$, and TiF_4 Precursors. Chem. Mater. **25**, 1656–1663 (2013).

110.Kuraitis, S., Kang, D., Mane, A. U., Zhou, H., Soares, J., Elam, J. W. & Graugnard, E. Atomic Layer Deposition of Sodium Fluoride Thin Films. J. Vac. Sci. Technol. A **39**, 032405 (2021).

111.Lee, Y., Dumont, J. W., Cavanagh, A. S. & George, S. M. Atomic Layer Deposition of AlF_3 Using Trimethylaluminum and Hydrogen Fluoride. J. Phys. Chem. C **119**, 14185–14194 (2015).

112.DuMont, J. W. & George, S. M. Competition Between Al_2O_3 Atomic Layer Etching and AlF_3 Atomic Layer Deposition Using Sequential Exposures of Trimethylaluminum and Hydrogen Fluoride. J. Chem. Phys. **146**, 052819 (2017).

113.Jackson, D. H. K., Laskar, M. R., Fang, S., Xu, S., Ellis, R. G., Li, X., Dreibelbis, M., Babcock, S. E., Mahanthappa, M. K., Morgan, D., Hamers, R. J. & Kuech, T. F. Optimizing AlF_3 Atomic Layer Deposition Using Trimethylaluminum and TaF_5: Application to High Voltage Li-ion Battery Cathodes. J. Vac. Sci. Technol. A **34**, 031503 (2016).

114.Hansen, P.-A., Zikmund, T., Yu, T., Nitsche Kvalvik, J., Aarholt, T., Prytz, Ø., Meijerink, A. & Nilsen, O. Single-step Approach to Sensitized Luminescence Through Bulk-embedded Organics in Crystalline Fluorides. Commun. Chem. **3**, 162 (2020).

115.Proslier, T., Klug, J. A., Elam, J. W., Claus, H., Becker, N. G. & Pellin, M. J. Atomic Layer Deposition and Superconducting Properties of NbSi Films. J. Phys. Chem. C **115**, 9477–9485 (2011).

116.Paramasivam, K. R., Radhakrishnan, M. & Balasubramanian, C. Dielectric Properties of Terbium Fluoride Thin Film Capacitors. Thin Solid Films **74**, 189–195 (1980).

117.Lingg, L. J. Lanthanide Trifluoride Thin Films: Structure, Composition, and Optical Properties. Academic Dissertation, University of Arizona (1990).

118.Jagadeesan, R. & Ramanujam, R. Structural and Electrical Characteristics of Vacuum Evaporated Gadolinium Fluoride Thin Films. J. Mater. Sci. Lett. **21**, 1341–1342 (2002).

119.Yao, S., Deng, W., Jin, J., Jin, C. & Li, C. Influence of Substrate Temperatures on the Properties of GdF_3 Thin Films with Quarter-wave Thickness in the Ultraviolet Region. Appl. Optics **54**, 5117–5122 (2015).

120.Thielsch, R., Heber, J., Uhlig, H. & Kaiser, N. Optical, Structural, and Mechanical Properties of Gadolinium Tri-fluoride Thin Films Grown on Amorphous Substrates. Proc. SPIE 5963, Advances in Optical Thin Films II, 211–222 (2005).

121.Mahalingam, T. & Radhakrishnan, M. Dielectric Relaxation in Gadolinium Fluoride Thin Films. J. Mater. Sci. Lett. **6**, 1135–1137 (1987).

122.Chang, Y. H., Wang, C. Y., Qi, L. Q. & Liu, H. Microstructure Related Properties of Gadolinium Fluoride Films Deposited by Molybdenum Boat Evaporation. IOP Conf. Ser. Earth Environ. Sci. **81**, 012036 (2017).

123.Wang, J., Maier, R., Dewa, P. G., Schreiber, H., Bellman, R. A. & Dawson-Elli, D. Nanoporous Structure of a GdF_3 Thin Film Evaluated by Variable Angle Spectroscopic Ellipsometry. Appl. Optics **46**, 3221–3226 (2007).

124.Sønsteby, H. H., Nilsen, O. & Fjellvåg, H. Atomic Layer Deposition of (K,Na)(Nb,Ta)O_3 Thin Films. J. Vac. Sci. Technol. A **34**, 041508 (2016).

125.Østreng, E., Sønsteby, H. H., Øien, S., Nilsen, O. & Fjellvåg, H. Atomic Layer Deposition of Sodium and Potassium Oxides: Evaluation of Precursors and Deposition of Thin Films. Dalton Trans. **43**, 16666–16672 (2014).

126.Atosuo, E., Heikkilä, M. J., Miikkulainen, V., Vehkamäki, M., Ritala, M. & Leskelä, M. "*In Situ High Temperature X-Ray Scattering Studies on Atomic Layer Deposited bilayers of A_2CO_3 and MO_x (A = Li/Na, M = Nb/Ti/Hf)*", E-MRS Fall Meeting 2017.

127.Väyrynen, K., Hatanpää, T., Mattinen, M., Heikkilä, M., Mizohata, K., Meinander, K., Räisänen, J., Ritala, M. & Leskelä, M. Diamine Adduct of Cobalt(II) Chloride as a Precursor for Atomic Layer Deposition of Stoichiometric Cobalt(II) Oxide and Reduction Thereof to Cobalt Metal Thin Films. Chem. Mater. **30**, 3499–3507 (2018).

128.Väyrynen, K. Hatanpää, T., Mattinen, M., Mizohata, K., Meinander, K., Räisänen, J. Link, J., Stern, R., Ritala, M. & Leskelä, M. Atomic Layer Deposition of Intermetallic Co_3Sn_2 and Ni_3Sn_2 Thin Films. Adv. Mater. Interfaces **6**, 1801291 (2019).

129.Mäntymäki, M., Ritala, M. & Leskelä, M., US9394609B2 (2016).

130.Jobin, F., Paradis, P., Ozan Aydin, Y., Boilard, T., Fortin, V., Gauthier, J.-C., Lemieux-Tanguay, M., Magnan-Saucier, S., Michaud L.-C., Mondor, S., Pleau, L.-P., Talbot, L., Bernier, M. & Vallée, R. Recent Developments in Lanthanide-doped Mid-infrared Fluoride Fiber Lasers. Opt. Express **30**, 8615 (2022).

131.Aronniemi, M., Saino, J. & Lahtinen, J. Characterization and Gas-sensing Behavior of an Iron Oxide Thin Film Prepared by Atomic Layer Deposition. Thin Solid Films **516**, 6110–6115 (2008).

132.Sønsteby, H. H., Bratvold J. E., Killi, V. A.-L. K., Choudhury, D., Elam, J. W., Fjellvåg, H. & Nilsen, O. Tert-butoxides as Precursors for Atomic Layer Deposition of Alkali Metal Containing Thin Films. J. Vac. Sci. Technol. A **38**, 060804 (2020).

133.Weiß, A., Popov, G., Atosuo, E., Vihervaara, A., Jalkanen, P., Vehkamäki, M., Leskelä, M., Ritala, M. & Kemell, M. Atomic Layer Deposition of CsI and $CsPbI_3$. Chem. Mater. **34**, 6087–6097 (2022).